The dispersive potential-vorticity dynamics of coastal outflows

M. Nguyen[1] and E. R. Johnson[1]

[1]Department of Mathematics, University College London, London, WC1E 6BT, UK

(Received xx; revised xx; accepted xx)

This paper discusses the propagation of coastal currents generated by a river outflow using a 1 $\frac{1}{2}$-layer, quasigeostrophic model, following Johnson *et al.* (2017) (JSM17). The model incorporates two key physical processes: Kelvin-wave-generated flow and vortical advection along the coast. We extend JSM17 by deriving a fully-nonlinear, long-wave, dispersive equation governing the evolution of the coastal current width. Numerical solutions show that at large times the flow behaviour divides naturally into three regimes: a steady outflow region, intermediate regions consisting of constant-width steady currents, and unsteady propagating fronts leading the current. The widths of the steady currents depend strongly on dispersion when the constant outflow potential vorticity anomaly is negative. Contour-dynamic simulations show that the dispersive equation captures the full quasigeostrophic behaviour more closely than JSM17 and gives accurate bounds on the widths of the steady currents.

Key words: Hydraulic control, Quasi-geostrophic flows, Waves in rotating fluids

1. Introduction

River outflows and their associated boundary fronts strongly influence the ocean and thermohaline circulation (Rahmstorf 2003), where less dense freshwater flows entering higher-density oceanic waters generate movement across the globe. Freshwater input from rivers introduced by the Arctic Ocean is observed to slow heat distribution throughout the Northern Hemisphere (Holliday *et al.* 2020). Piecuch *et al.* (2018) examine how variable river discharge influences oceanic circulation, contributing to rising sea levels on the East Coast of the United States. Moreover, the mixing of ocean and coastal waters generated by outflow currents determines nutrient transport and the subsequent distribution of phytoplankton populations (Ajani *et al.* 2020). Sun *et al.* (2022) specifically emphasise how complex interactions between different river flows affect the distribution of the phytoplankton community in coastal waters of South Korea. On a smaller scale, the Hawkesbury River estuary in Australia is a source of nutrient-dense waters transported by the river plume (Li *et al.* 2022), directly influencing the marine taxonomy of the river mouth. Wang *et al.* (2022) note that coastal and estuarine fronts led by river discharges cause the accumulation of pollutants and microplastics.

There is growing evidence to causally relate increasing river discharge to rising coastal sea levels, as currents can be trapped along the coast. With the intensifying hydrological cycle (Pratap & Markonis 2022), Tao *et al.* (2014) predict up to a 60% increase in discharge from the Mississippi River basin over the next century, the largest source of water drainage from North America into the Atlantic Ocean. Similarly, Piecuch *et al.*

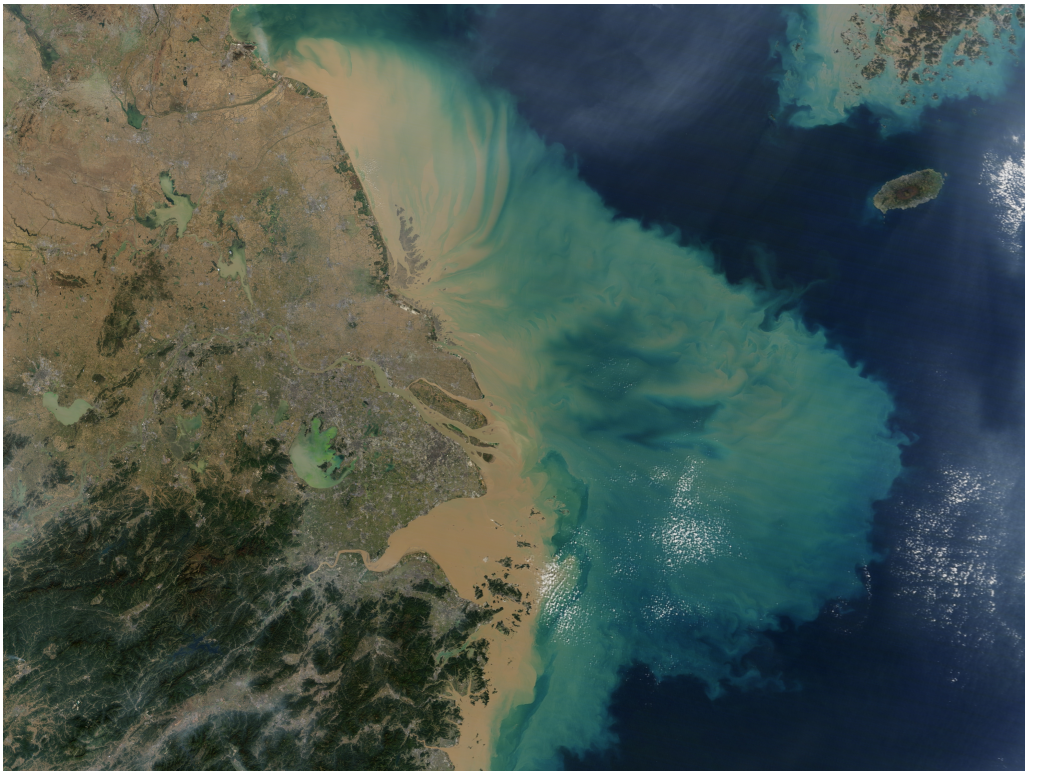

Figure 1: Winter sediment plumes from the Yangtze River spreading into the East China Sea forming a "shelf" of water stretching leftwards (data from the MODIS satellite, 2017), made visible by tidal stirring of bottom sediments (Luo *et al.* 2017).

(2018) suggest from Atlantic and Gulf coast data that river discharge is responsible for up to 15% of the annual sea-level variance.

Numerical studies of river outflows (Mestres *et al.* 2007) examine how changes in river width, inlet transport, and the Coriolis parameter affect the surface plume width given a constant outflow discharge. Tides, wind forcing, and unsteady outflows can also influence the evolution of the coastal front (Southwick *et al.* 2017). In the Northern Hemisphere freshwater from rivers could be expected to turn right (in the direction of the Coriolis force). There are, however, clear indicators of leftward propagation, such as the suspended sediments that form the Yangtze River plume front (figure 1). Johnson *et al.* (2017, JSM17 herein) capture both phenomena by using a theoretical long-wave approximation to the $1\frac{1}{2}$-layer, quasigeostrophic (QG) equations where fluid expelled from a single-channel outflow is driven by a Kelvin wave (KW) and vortical advection along the coast. More sophisticated 2-layer outflow models describing the discharge of the Ganges-Brahmaputra-Meghna mega-delta (Kida & Yamazaki 2020), a major freshwater source in the Bay of Bengal, show how fronts from individual river branches that form the delta, are crucial in the overall outflow dynamics.

Jamshidi & Johnson (2019) modify JSM17 using the semigeostrophic equations (SG) to investigate the validity range in the QG approximation. The modification admits a KW propagating along the coast at a finite speed in contrast to the QG limit where the KW propagates infinitely fast. While the SG equations admit Rossby numbers of order unity, the outflow behaviour remains qualitatively similar. Thus, we continue with the simpler

QG model, but capture further detail in the solutions by studying the dispersive long-wave PV equation which adds first-order terms to the hydraulic PV equation in JSM17. This addresses the incomplete predictions of the hydraulic theory for narrow source outflows and predicts new behaviour, such as the formation of dispersive shock waves (DSWs) under certain parameters of the coastal outflow problem. The analysis builds on the methods in Jamshidi & Johnson (2020, JJ20 herein) who derive the dispersive equation for a coastal current of constant flux along a wall, and analyse the Riemann problem for the adjustment of a step change in the width of an alongshore current using El's dispersive-shock fitting technique (El 2005).

Section 2 describes the idealised flow geometry considered here, governed by the $1\frac{1}{2}$-QG equations, and presents the leading-order hydraulic limit of the equations and their first-order dispersive correction. Away from the source, the system supports travelling waves of fixed form and the equations governing these are noted in §2.3. The flow evolves to divide naturally at large times into three regimes: a steady region containing the outflow, constant-width currents leading away from the outflow regions, and unsteady propagating frontal regions leading the constant-width currents. Section 3 considers the outflow region, presenting numerical solutions for the asymptotically steady flow there and discussing the transition between subcritical and supercritical flow across the outflow. The widths of the outflow currents for negative PV outflows are shown to depend strongly on the strength of the dispersion. Section 4 describes the various compound wave structures observed in the fronts leading the constant-width currents, and §5 compares predictions from the dispersive long-wave theory with integrations of the full QG equations. The results are summarised briefly in §6.

2. Formulation

We consider a river outflow model where fluid is released from a constant depth inlet and flows along the coast into a half-space consisting of an upper active layer, comprising the expelled fluid and displaced ambient ocean water, and an ambient lower layer of infinite depth. The problem setup is shown from a plan view in figure 2(a) and a side view in figures 2(b)(i), 2(b)(ii). We take Cartesian coordinates $\mathcal{O}xyz$, with x along the coast, y offshore, and z vertical. The system is rotating with Coriolis parameter f about the z-axis. Here, D_s denotes the inlet depth, D the depth of the upper ambient fluid, and L denotes the half-width of the outflow lying along a vertical coast $y = 0$. We denote the connected region of the expelled fluid as $\mathcal{D}$ which is bounded by the contour $\mathcal{C}$ separating the expelled fluid from the ambient. At time $t > 0$, fluid is released from the outflow into the half-space $y > 0$ with a constant discharge rate that is independent of the width of the source and constant non-zero potential vorticity (PV) denoted by $\Pi^\star$. The expelled and ambient fluid in the upper layer has density ρ_1 while the lower layer has zero PV and density $\rho_2 > \rho_1$, with $|\rho_1 - \rho_2| \ll \rho_2$ so the Boussinesq approximation is valid. This layered system satisfies the $1\frac{1}{2}$-layer QG equations provided the relative depth change between the inlet and the active layer is small, i.e., $|D - D_s| \ll D$. Typical velocities are small compared to the speed of long free-surface water waves, so the surface $z = 0$ can be taken as effectively rigid with the dynamics restricted to the interface between the layers. The difference between the potential vorticity of the expelled fluid and the upper ambient fluid, defined as the potential vorticity anomaly (PVa), $\Pi_0 := \Delta\Pi^\star = f/D_s - f/D$, is positive if the outflow depth is deeper than the inlet depth $D_s < D$, or negative if $D_s > D$. Herein (as in JJ20) we denote PVa as just PV for brevity.

We consider the case where the coastal front $\mathcal{C}$ does not overturn so the frontal width can be expressed as $y = Y(x, t)$. This is true for gently propagating coastal fronts but

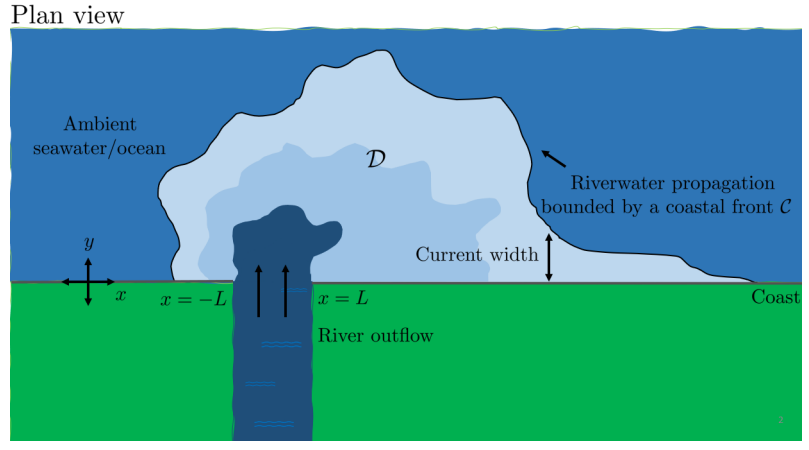

(a)

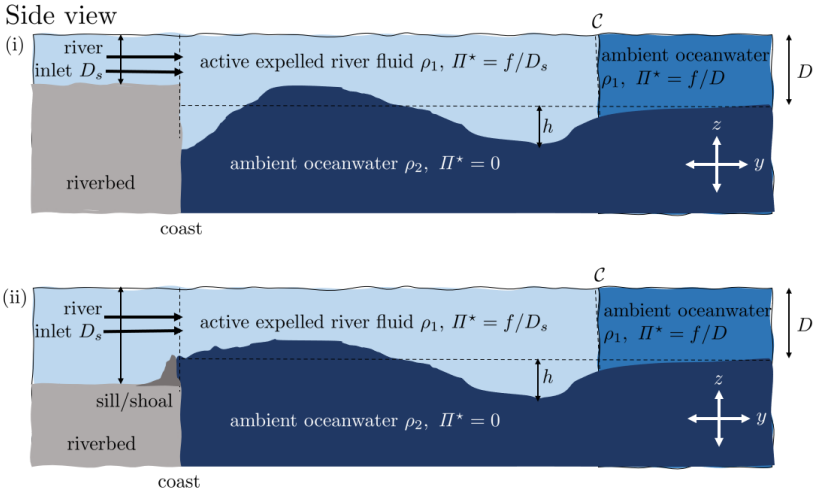

(b)

Figure 2: A schematic of a river outflow expelling fluid at $t > 0$ from an inlet with depth D_s into the upper layer of depth D. The lower layer of ambient ocean water below has infinite depth hence $\Pi^\star = 0$. The subsequent displacement of the interface between the layers is denoted by h. (a) the plan view of a river source of half-width L where the expelled fluid evolves to form a region $\mathcal{D}$ enclosed by a closed coastal front $\mathcal{C}$ (including the coast boundary $y = 0$). (b) the side-view where (b)(i): the outflow depth is deeper than the river inlet, so there is positive PV(a) generation. (b)(ii): outflow depth is shallower than the inlet (due to the presence of a shoal say) so there is negative PV(a) generation.

contour-dynamical integrations of the full QG equations in §5 suggest that overturning can occur, particularly for flows begun impulsively, and is discussed separately. In our QG framework, we introduce a streamfunction

$$\psi(x, y, t) = \frac{g' h(x, y, t)}{f Q_0}, \tag{2.1}$$

where $h(x, y, t)$ is the interface displacement. The time-dependent evolution of $\mathcal{C}$ is governed by the QG equation for ψ. Here, Q_0 is the area flux expelled by the outflow (with total volume $Q_0 D$), g' is the reduced gravity, with the horizontal velocities of the

flow given by $(u, v) = (-\psi_y, \psi_x)$. Spatial and temporal scales are nondimensionalised (with choices justified, along with other quantities below, in JSM17) according to the vortex length L_v and advection timescale T_v where

$$L_v = (Q_0/|\Pi_0 D|)^{1/2}, \qquad T_v = L_v^2/Q_0. \tag{2.2}$$

We define W to be the nondimensionalised half-width (herein just width) of the outflow such that $W = L/L_v$. The nondimensional governing equation becomes

$$q = \nabla^2\psi - \frac{1}{a^2}\psi = \begin{cases} 0 & y > Y(x,t) \\ \Pi & 0 < y < Y(x,t), \end{cases} \tag{2.3}$$

where $\nabla^2 = \partial/\partial x^2 + \partial/\partial y^2$ is the Laplacian operator, the constant PV is nondimensionalised $\Pi = \Pi_0/|\Pi_0|$ so that positive PV is $\Pi = +1$ and negative PV is $\Pi = -1$, and $a = L_R/L_v$ is the ratio of the Rossby radius of deformation for the interface $L_R = \sqrt{g'H}/f$ to the vortical length scale L_v. The parameter a is later referred to as simply the Rossby radius. It measures the ratio of the strength of advection by the image vorticity effect to that by the Kelvin-wave induced flow. If $\Pi = +1$, then the advection of the fluid combines with the Kelvin wave to reinforce the turning effect. If $\Pi = -1$, the image effect opposes the Kelvin wave.

We denote the flux function of the source outflow by $Q(x)$ with width W along the coast $y = 0$. The fluid is impulsively expelled at $t > 0$ given by the no-flux boundary condition (2.4), and far from the coast the fluid is stationary so

$$\psi(x, 0, t) = Q(x), \tag{2.4}$$

$$\psi \to 0, \quad y \to \infty, \tag{2.5}$$

Here $Q(x)$ is normalised so $Q(x \leqslant -W) = 0$, $Q(x \geqslant W) = 1$. The remaining condition is the kinematic boundary condition so that fluid particles on the coastal front remain on the coastal front $\mathcal{C}$,

$$Y_t = [\psi(x, Y(x,t))]_x. \tag{2.6}$$

2.1. *The leading-order hydraulic solution*

Rescaling (2.3) using the long-wave variables

$$X = \varepsilon x, \quad T = \varepsilon t,$$

where $\varepsilon = 1/W$, and expanding ψ in terms of ε gives

$$\psi(X, y, T) = \psi^0 + \varepsilon^2\psi^1 + \mathcal{O}(\varepsilon^4). \tag{2.7}$$

We substitute (2.7) into (2.3) which is matched with the leading-order ε^0 and first-order ε^2 terms. This derivation is summarised from JJ20, with the modification that $Q(x)$ here varies instead of being constant in x. Directly evaluating ψ^0 at the coastal front $y = Y(X, T)$ gives

$$\psi^0(X, Y, T) = Q_e(X, Y, T) = -\frac{a^2\Pi}{2} + (Q(X) + a^2\Pi)e^{-Y/a} - \frac{\Pi a^2}{2}e^{-2Y/a}. \tag{2.8}$$

$Q_e(X, Y, T)$ represents the net transport of the (ambient) oceanic fluid from point X. The kinematic boundary condition (2.6) at the leading order becomes

$$Y_t + \left[\left(\frac{Q(x)}{a} + a\Pi\right)e^{-Y/a} - a\Pi e^{-2Y/a}\right]Y_x + Q'(x)e^{-Y/a} = 0, \tag{2.9}$$

reconverting from $(X,T)\to(x,t)$ and its respective derivatives. Equation (2.9) governs the leading-order behaviour of the coastal front at $y=Y(X,T)$, described here as the hydraulic solution.

2.2. *The first-order dispersive correction*

The next order in ε gives the first order correction of ψ at $y=Y(X,T)$ as

$$\psi^1(X,Y,T)= \\ -\frac{a^3\Pi}{4}Y_{XX}+\left(\frac{a^2}{2}\Pi Y Y_{XX}+\frac{a^3}{4}\Pi Y_{XX}-\frac{a\Pi}{2}Y(Y_X)^2\right)e^{-2Y/a}+\frac{a}{2}Q_{XX}(X)Ye^{-Y/a}. \tag{2.10}$$

The dispersive kinematic boundary condition (2.6) including first-order terms becomes

$$Y_t+\left[\frac{a^2\Pi}{2}e^{-2Y/a}-\left(Q(x)+a^2\Pi\right)e^{-Y/a}\right]_x \\ +\frac{a^3\Pi}{4}Y_{xxx}-\Pi\left[\left(\frac{a^2}{2}YY_{xx}-\frac{a}{2}Y(Y_x)^2+\frac{a^3}{4}Y_{xx}\right)e^{-2Y/a}\right]_x-\left[\frac{a}{2}Q_{xx}(x)Ye^{-Y/a}\right]_x=0. \tag{2.11}$$

Expanding (2.11) gives the alternative form of the first-order dispersive kinematic boundary condition

$$Y_t+\left[\left(\frac{Q(x)}{a}+a\Pi\right)e^{-Y/a}-a\Pi e^{-2Y/a}\right]Y_x \\ +\frac{a^3\Pi}{4}Y_{xxx}-\Pi\left((Y-a/2)(Y_x)^3+\frac{a^3}{4}Y_{xxx}+\frac{a^2}{2}YY_{xxx}-2aYY_xY_{xx}\right)e^{-2Y/a} \\ -Q_x(x)e^{-Y/a}-\frac{a}{2}Q_{xxx}(x)Ye^{-Y/a}-\frac{a}{2}Q_{xx}(x)\left(1-Y/a\right)Y_xe^{-Y/a}=0, \tag{2.12}$$

again reconverting from $(X,T)\to(x,t)$. While the parameter ε no longer appears, the variables x,t vary slowly. Formally, this means $1/\varepsilon\equiv W\gg 1$ and a is of order unity. When $Q(x)$ narrows to a point source outflow $W\to 0$, its derivatives become large $Q_x(x)\sim 1/W\gg 1$, which violates this requirement. Nevertheless, this system can still be treated with surprisingly good accuracy in §3.2.

2.3. *The travelling wave solutions of the dispersive equation*

Provided the flux function is constant $Q(x)\equiv Q$ (in the regions $|x|>W$), the system supports waves of permanent form as noted in JJ20. We change to moving coordinates by setting $\xi=x-st$ and looking for solutions in a steady frame, the governing PV equation (2.12) can be written in potential form

$$(Y_\xi)^2=\frac{2}{a^2}\frac{a^3e^{-2Y/a}-4a(Q\Pi+a^2)e^{-Y/a}+2s\Pi Y^2+\alpha Y+E}{a-(a+2Y)e^{-2Y/a}}\equiv\frac{2}{a^2}\frac{\nu(Y,s,\alpha,E)}{\mathcal{G}(Y)}, \tag{2.13}$$

where α,E are the constants of integration, and s is the speed of the travelling wave. JJ20 describe the different types of nonlinear travelling waves and the criteria for their formation for the case $Q=1$. We focus on the soliton and kink soliton waves for arbitrary but constant Q: a soliton wave is a single wavepacket of amplitude given by $|Y_\infty-Y_1|$ maintaining its shape, propagating along some background $Y=Y_\infty$ value, with

conditions given by

$$\nu(Y = Y_1) = 0,\ \nu(Y = Y_\infty) = 0,\ \nu'(Y = Y_\infty) = 0, \tag{2.14}$$

where $'$ denotes differentiation with respect to Y. Two far-field states of Y say Y_1 and Y_2 may be connected by a kink soliton, often regarded as a "half-soliton" (as opposed to a soliton which returns to its background value). A special case of a kink soliton is a coastal intrusion which is a current of constant width Y_I terminating at the coast $Y = 0$. From JJ20, the intrusion meets the coast smoothly adding one more condition

$$\nu(Y = 0) = 0,\ \nu'(Y = 0) = 0,\ \nu(Y = Y_I) = 0,\ \nu'(Y = Y_I) = 0. \tag{2.15}$$

This determines the constants α, E, as well as giving the unique speed s_I and the width of the intrusion Y_I determined by solving the equations

$$\begin{aligned}(-a^2Y_I + 3a^3 + 4aQ\Pi - 2Q\Pi Y_I)e^{2Y_I/a} - (2a^2Y_I + 4a^3 + 4aQ\Pi + 2Q\Pi Y_I)e^{Y_I/a}\\ +(a^2Y_I + a^3) = 0,\end{aligned} \tag{2.16}$$

$$s_I = \frac{-2a^2e^{-2Y_I/a} + 4(a^2 + Q\Pi)e^{-Y_I/a} - 2a^2 - 4Q\Pi}{-4Y_I\Pi}, \tag{2.17}$$

such that the PV front meets the coast with finite gradient

$$(Y_\xi)^2|_{Y=0} = \frac{2\Pi(as_I - Q)}{a^2}. \tag{2.18}$$

The parameters a, Q and Π determine the speed, s_I and width, Y_I, of the intrusion.

3. The outflow region

For steady flow, (2.6) integrates directly to give

$$F(Y, Y_x, Y_{xx}) := \psi^0(x, Y) + \psi^1(x, Y, Y_x, Y_{xx}) = \Phi, \tag{3.1}$$

where Φ is a constant. In the far field $|x| \to \infty$, the PV front settles to a constant-width current (upstream width denoted by Y_- and downstream width Y_+) and the full solution there becomes identical to the hydraulic solution, as noted below in §3.1.

We solve (2.12) as a boundary value problem (BVP) in steady flow. By selecting the solution that satisfies the condition $dY/dx = 0$ up or downstream (depending on the sign of Π), this uniquely determines the solution that omits waves incident on the constant-width current region. We focus (for reasons discussed in §3.1.2) on the case $\Pi = -1$, where the constant $\Phi \equiv Q_e(x = -W)$ is set so that the upstream current width at $Q = 0$ can be rewritten as $Y(-W) \equiv Y_-$.

Outside the source $x > W$, the steady dispersive PV equation is rewritten in potential form where $s = 0$ in (2.13). This introduces a truncated or partially complete soliton where the current width decays exponentially towards the far-field Y_+ width for $\Pi = -1$.

The steady problem for $\Pi = -1$ is thus

- $Y = Y_-; \quad x < -W,$ (3.2)
- $\psi^0(x, Y) + \psi^1(x, Y, Y_x, Y_{xx}) = \Phi; \quad |x| \leqslant W$ (3.3)
  $\Phi = Q_e(x = -W), \quad Y_x(-W) = 0, \quad Y_x(W)^2 = \dfrac{2}{a^2}\dfrac{\nu(Y(W), \alpha_+, E_+)}{\mathcal{G}(Y(W))},$
- $(Y_x)^2 = \dfrac{2}{a^2}\dfrac{\nu(Y, \alpha_+, E_+)}{\mathcal{G}(Y)}; \quad x > W.$ (3.4)

The constants α_+, E_+ are determined using the conditions for the existence of soliton in (2.14) at $Y = Y_+$, $\Pi = -1$, and solving (3.3) in the outflow region $|x| \leqslant W$ gives the value of $Y(W) \equiv Y_+$ and Φ, allowing (3.4) to be solved from $x = W$. Knowledge of Φ uniquely determines the widths of the far-field Y_+, Y_- and by extension the entire steady system.

We solve the steady equation using the method of Jamshidi & Johnson (2021) by truncating the domain to some $x = \pm L$ for large L using a BVP solver (bvp4c/bvp5c) in MATLAB. Equation (3.3) is solved across the entire domain, setting the flux function to be $Q(x) := Q_4(x)$ in (4.1), which is equivalent to solving (3.2), (3.3), (3.4) separately in each domain and unifying the solutions. Although a shooting method can be used to find Φ similarly done in Jamshidi & Johnson (2021), this is automatically handled in the bvp4c/bvp5c solvers by introducing one more equation,

$$\Phi = Q_e(x = -W) = \frac{-a^2\Pi}{2}(Q + a^2\Pi)e^{-Y_-/a} - \frac{\Pi a^2}{2}e^{-2Y_-/a}, \tag{3.5}$$

that must be satisfied alongside the ODE. Figure 3 gives an example of the numerical simulation.

3.1. *Hydraulic and dispersive control*

Consider a steady solution $Y \equiv Y_s(x)$ of (2.12). Perturbing the solution with small waves say

$$Y = Y_s(x) + \hat{\varepsilon}y, \quad y \sim \mathcal{O}(1) \tag{3.6}$$

where $\hat{\varepsilon} \ll 1$, substituting this into (2.12) and discarding terms smaller than order $\hat{\varepsilon}$ gives the equation

$$\frac{\partial y}{\partial t} + C\frac{\partial y}{\partial x} = f\,(y)\,, \; C = (C^0 + C^1), \tag{3.7}$$

$$C^0 = \left(\frac{Q(x)}{a} + a\Pi\right)e^{-Y_s/a} - a\Pi e^{-2Y_s/a} \sim \mathcal{O}(1), \tag{3.8}$$

$$C^1 = -\Pi\left(3\left(Y_s - \frac{a}{2}\right)(Y_s')^2 - 2aY_sY_s''\right)e^{-2Y_s/a} - \frac{a}{2}Q''(x)\,(1 - Y_s/a)\,e^{-Y_s/a} \sim \mathcal{O}(\hat{\varepsilon}^2). \tag{3.9}$$

To remain in the long-wave regime we require $\hat{\varepsilon}y$ to be much smaller than a typical disturbance wavelength, and strictly f is a function of y_{xx}, $y_{xxx} \sim \mathcal{O}(\hat{\varepsilon}^2)$, $\mathcal{O}(\hat{\varepsilon}^3)$ that is disregarded. Keeping terms $\mathcal{O}(\hat{\varepsilon})$ or greater only, we view (3.7) as a forced first-order partial differential equation (PDE) with a disturbance propagation speed $C = C^0 + \mathcal{O}(\hat{\varepsilon}^2)$, so C^0 is regarded as the locally constant long-wave speed of the dispersive equation at a given point. In the context of steady-flow hydraulics, the flow is supercritical where

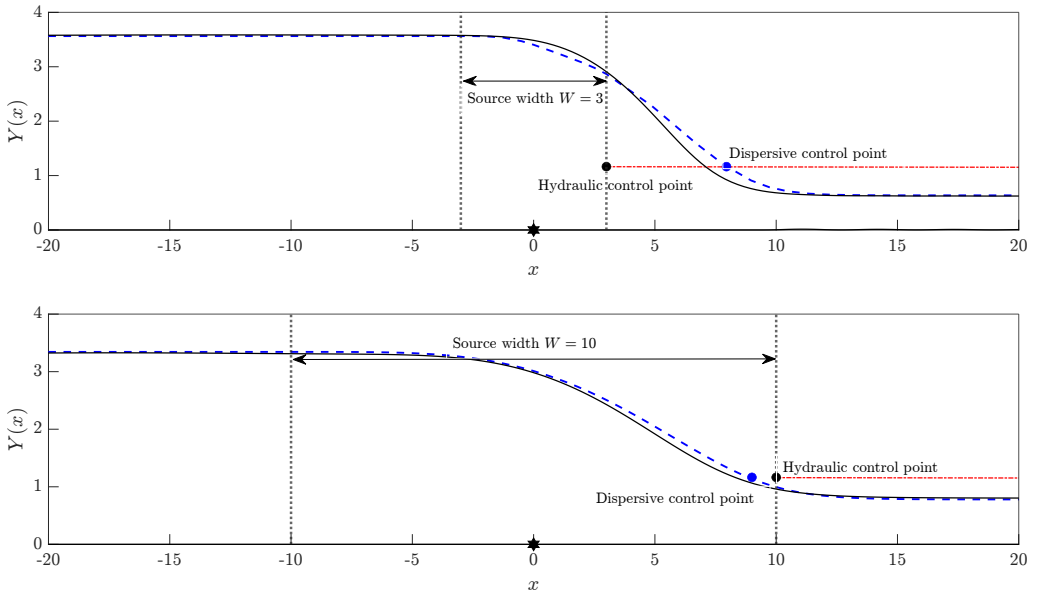

Figure 3: The steady dispersive solutions (shown in blue) for $a = 1.3$, $\Pi = -1$ plotted for source widths: top) W=3, bottom) W=10 with the outflow centred at $x = 0$ (marked as a filled star). For comparison the full QG solutions (in black) is shown for $t = 500$. The locations of the hydraulic and dispersive control point are shown by a black and blue filled circle respectively. The red line denotes the hydraulic rarefaction at $t = 10000$, an almost constant-width current extending from the hydraulic control point.

$C > 0$ and subcritical where $C < 0$. The parts where $C = 0$ give critical control and we denote its location by the control point $x = x_c$.

3.1.1. *The $\Pi = -1$ case*

First, considering the hydraulic PV equation (2.9) and summarising the results in JSM17, the steady solution selects the condition in which the control point is fixed at the downstream edge $x_c = W$ of the source, determining Y_+. The controlled solution at $x_c = W$ also establishes the size of the steady constant-width current upstream Y_-. In the hydraulic context, condition (3.1) simplifies to

$$Q_e(Y = Y_-, Q = 0, \Pi) = Q_e(Y = Y_+, Q = 1, \Pi) = \Phi, \tag{3.10}$$

recalling $Q_e \equiv \psi^0$ is the leading-order (hydraulic) streamfunction evaluated at the PV front. Requiring flow to be critically controlled gives some essential conditions in the hydraulic equation. Upstream at $Q = 0$ the long-wave speed $C(Y)|_{Q=0} < 0$ holds for all Y, therefore, we always have steady supercritical flow in this region. The $Q = 1$ region downstream must transition to subcritical flow, which means that there is a critical point in between $C(Y) = 0$. This is used to determine Y_+ and we can derive the minimum value of Y_- in our equation using (3.10)

$$Y_+ := (Y_+)_{hyd,\ -1} = a \ln\left(\frac{a^2}{a^2-1}\right), \quad Y_- := (Y_-)_{hyd,\ -1} = a \ln\left(\frac{a^4 + a^2\sqrt{2a^2-1}}{(a^2-1)^2}\right). \tag{3.11}$$

When $a \leqslant 1$, Y_-, Y_+ diverges (or becomes negative or undefined), hence steady solutions are only possible for $a > 1$.

Similar behaviours occur in the dispersive PV equation, as (3.10) holds in the constant-

width current regions. Upstream of the source outflow $x < -W$, as with the hydraulic equation, there is supercritical flow $C < 0$; thus, any Rossby waves that form must propagate away from the coastal front. In this region, the hydraulic terms dominate the front and $C^1 \equiv 0$. It follows that the upstream current is constant-width where waves cannot stand, hence we can set $dY/dx = 0$ at $x = -W$.

The control point is fixed at $x_c = W$ in the hydraulic prediction and so the current widths Y_-, Y_+ do not change with the outflow width. Jamshidi & Johnson (2021) describes a PV front involving a topographic symmetrical shelf (of a different fixed depth to the seabed) in which the dispersive prediction selects the critical condition $C = 0$ exactly at the peak of the topographic perturbation $x = 0$. In the context of this dispersive PV equation, the control point is also influenced by the width of the outflow, so the position of the control point can no longer be determined a priori.

Figure 3 compares the numerical steady solution with the full problem (using the contour dynamics method of §5), which are run until Y_-, Y_+ converges to its steady value. The widths $Y_\pm$ are well predicted for source widths $W = 3$, $W = 10$. This is a significant improvement to the hydraulic rarefactions (red), although there are some discrepancies in the dispersive wave (less so for $W = 10$) that links Y_- to Y_+ compared to the full problem. Note that the Y locations of the hydraulic and dispersive control points are virtually identical (with $\mathcal{O}(\hat{\varepsilon}^2)$ error), but as the solutions differ, these control points lie on different x values. Here, the dispersive control point (blue) is not necessarily fixed at the outflow edge $x = W$ unlike the hydraulic control point (black). This allows it to match the widths of the full solutions. For the larger width outflow, the control point lies closer to the downstream outflow as it converges to the hydraulic rarefaction.

3.1.2. *The $\Pi = +1$ case*

Critical control for $\Pi = +1$ in the hydraulic solution occurs at the edge of the source outflow $x = -W$, when there is no current upstream. As shown in JSM17, this gives remarkably accurate results compared to the full problem, predicting the upstream and downstream steady currents as

$$(Y_-)_{hyd,\ +1} \equiv 0, \quad (Y_+)_{hyd,\ +1} = a \ln\left(1/a^2 + 1 + \sqrt{1/a^4 + 2/a^2}\right). \tag{3.12}$$

The dispersive equation also establishes its own control point but this causes the front to lie below the coast, i.e., reach negative Y values. From §3.3, these solutions are not valid and must be omitted when comparing them to the full problem. The dispersive PV equation is therefore only useful in predicting current widths Y_-, Y_+ when $\Pi = -1$.

3.2. *The narrow source limit, $W \to 0$*

The governing PV equation (2.12) is not formally valid for narrow outflows $W \ll \mathcal{O}(1)$. However, over long times, the dispersive equation for $\Pi = -1$ captures the far-field values (Y_-, Y_+) of the full problem well in these regimes (figure 4). Therefore, it is useful to analyse the dispersive equation here and extend the analysis of (2.12) to all W.

In §3 for $\Pi = -1$, the far-field currents Y_+, Y_- are joined together by the outflow region as follows: a (truncated) soliton formed by the outflow region connects the downstream constant-width current Y_+ to an intermediate point $Y = Y_s$ at $x = W$. This point Y_s smoothly links to the constant-width current $Y(x = -W) = Y_-$ within the outflow region $|x| < W$ to $x = -W$. As the source width becomes arbitrarily small $W \to 0$, the ODE can no longer smoothly adjust the soliton to Y_- and must undergo a shock at $x = 0$ instead. The soliton becomes truncated exactly at its maximum point to minimise the width of the shock, so the derivative Y_x is zero at $x = 0$. Figure 5 illustrates the shape

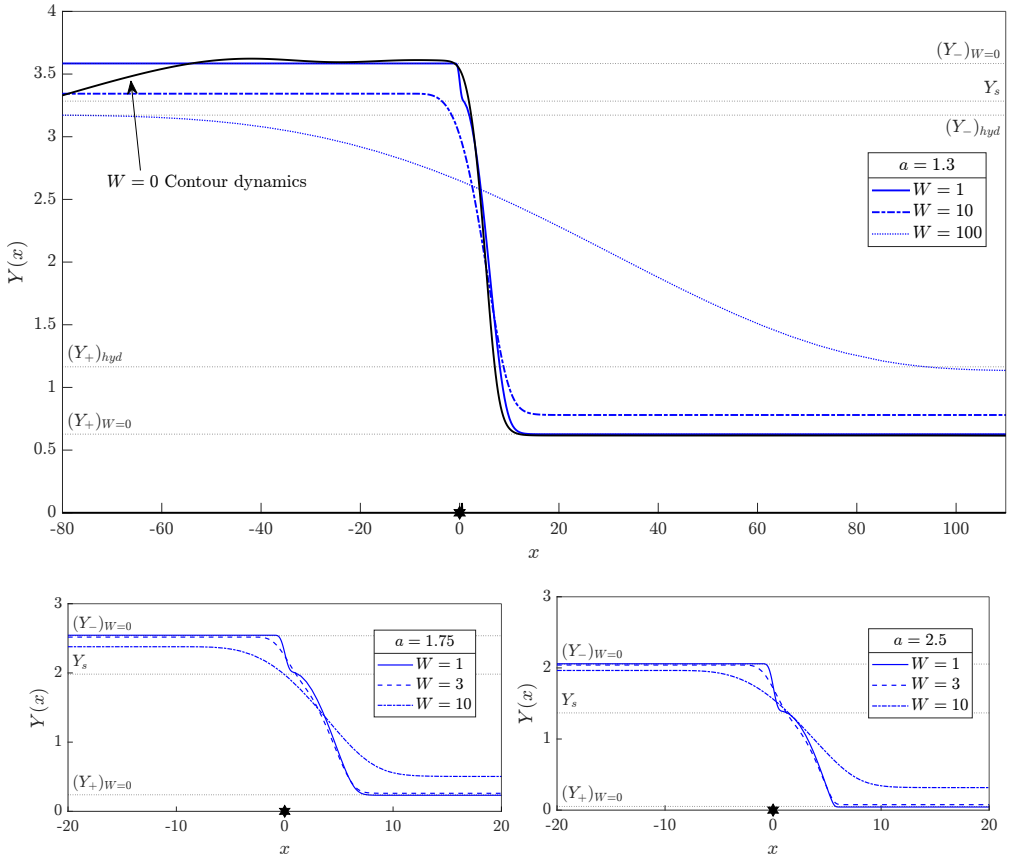

Figure 4: Top): The steady dispersive solutions (blue) at $a = 1.3$, $\Pi = -1$ shown for different widths $W = 1,\ 10, 100$, compared directly to the contour dynamics at $W = 0$ at $t = 1000$ (shown in black). Also overlaid is the comparison (dotted lines) with the hydraulic and dispersive predictions of the current widths $(Y_\pm)_{hyd}$, $(Y_\pm)_{W=0}$. bottom): as in top) but for $a = 1.75$ and $a = 2.5$ respectively ($W = 1,\ 3,\ 10$).

of the coastal front given a point source outflow. Overall, we stipulate that as $W \to 0$, $Y(x)$ satisfies

$$Y(x \to 0^-) = Y_-, \quad Y(x \to 0^+) = Y_s, \quad Y_x(x \to 0^-) = 0, \quad Y_x(x \to 0^+) = 0, \tag{3.13}$$

provided $\Pi = -1$, and Y_s denotes the width of the soliton from the coast.

We choose a smooth and monotonic normalised outflow $Q(x)$ with extremely small width W that converges to a point source. Integrating the steady form of (2.11) once gives

$$\frac{a^3\Pi}{4}Y_{xx} - \Pi\left[\left(\frac{a^2}{2}YY_{xx} - \frac{a}{2}Y\left(Y_x\right)^2 + \frac{a^3}{4}Y_{xx}\right)e^{-2Y/a}\right] - \frac{a}{2}Q''(x)Ye^{-Y/a} + \frac{a^2\Pi}{2}e^{-2Y/a} - \left(Q(x) + a^2\Pi\right)e^{-Y/a} - \Phi = 0, \tag{3.14}$$

with the constant of integration $\Phi = Q_e(Y_-)$. Integrating (3.14) from $-W$ to W with respect to x in the limit $W \to 0$ implies that the integral involving the last line of (3.14) vanishes as the integrand is bounded. Since $Y_x = 0$ at $x = \pm W$ following (3.13) then

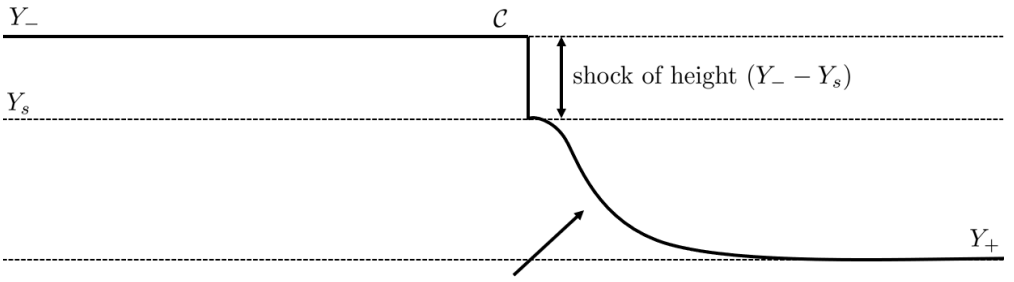

Figure 5: The suggested structure of the coastal front $\mathcal{C}$ for $\Pi = -1$ as the outflow width $W \to 0$ in dispersive flow. A shock links the constant-width current in $x < 0$ to a soliton asymptoting to Y_+.

the first term in the first line of (3.14) also becomes zero. After some simplification, we arrive at the expression

$$\lim_{W\to 0}\int_{-W}^{W}\left\{\frac{\Pi a}{4}\left[(2Y+a)e^{-2Y/a}\right]Y_{xx}+Q''(x)Ye^{-Y/a}\right\}\,dx=0. \tag{3.15}$$

Denoting the shock width or jump in $Y(x)$ across $x=0$ by $\langle Y\rangle$, we define

$$\langle Y\rangle=\lim_{W\to 0}[Y(W)-Y(-W)]=Y_- - Y_s, \tag{3.16}$$

so $\langle Q\rangle = 1$. Now considering the indefinite integral of (3.14) from $-W$ to x, then integrating once more from $-W$ to W as $W \to 0$, integrating by parts and simplifying using (3.15) gives

$$\begin{aligned}&\frac{a^2\Pi}{2}\langle Y\rangle+\frac{\Pi a^2}{4}\langle (Y+a)e^{-2Y/a}\rangle\\ &+\lim_{W\to 0}\int_{-W}^{W}x\left\{\frac{\Pi a}{4}\left[(2Y+a)e^{-2Y/a}\right]Y_{xx}+Q''(x)Ye^{-Y/a}\right\}dx=0.\end{aligned} \tag{3.17}$$

In the limit $W \to 0$, where $\delta(x)$ is the Dirac delta function,

$$Y''(x)\to\langle Y\rangle\delta'(x),\quad Q''(x)\to\delta'(x), \tag{3.18}$$

holds true, so simplifying (3.17) gives the required jump condition

$$\frac{a^2\Pi}{2}\langle Y\rangle+\frac{\Pi a^2}{4}\langle (Y+a)e^{-2Y/a}\rangle-\frac{\Pi a}{4}\langle Y\rangle\left[(2Y+a)e^{-2Y/a}\right]_{x=0}-\left[Ye^{-Y/a}\right]_{x=0}=0, \tag{3.19}$$

where for any $g(Y)$, we define $[g(Y)]_{x=0}$ as

$$[g(Y)]_{x=0}=\left[g(Y_-)+g(Y_s)\right]/2. \tag{3.20}$$

We have the first equation (3.19) to solve the three unknowns (Y_-, Y_s, Y_+). Next, we introduce a steady soliton in the constant $Q = 1$ region by imposing the conditions (2.14) derived from the travelling-wave solutions of the dispersive PV equation. We also stipulate the soliton joins to $Y_s \neq Y_+$, which gives the second equation

$$a^3e^{-2Y_s/a}-4a(a^2-1)e^{-Y_s/a}+\alpha_+Y_s+E_+=0, \tag{3.21}$$

with the constants α_+, E_+ determined from (2.14).

Since Y_+, Y_- are linked by the hydraulic flux function $Q_e(Y) = \Phi$, the final equation is given by

$$(1-a^2)e^{-Y_+/a} + \frac{a^2}{2}e^{-2Y_+/a} = -a^2 e^{-Y_-/a} + \frac{a^2}{2}e^{-2Y_-/a} = \Phi, \tag{3.22}$$

thus solving (3.19), (3.21), (3.22) simultaneously gives the values of (Y_-, Y_+, Y_s) for $\Pi = -1$, where we demand $Y_+ \leqslant Y_s < Y_-$. This shock is an unphysical artefact that predicts the correct (Y_-, Y_+) found in the numerical solutions of the full problem.

Together the steady hydraulic and dispersive $W \to 0$ width predictions form the upper or lower bounds of $Y_\pm$ at $\Pi = -1$ such that

$$\begin{aligned} (Y_-)_{W=0,\ -1} &:= (Y_-)_{max,\ -1}, \quad (Y_-)_{hyd,\ -1} := (Y_-)_{min,\ -1} \\ (Y_+)_{W=0,\ -1} &:= (Y_+)_{min,\ -1}, \quad (Y_+)_{hyd,\ -1} := (Y_+)_{max,\ -1}, \end{aligned} \tag{3.23}$$

where *hyd* refers to the hydraulic predictions, giving an upper (*max*) and lower bound (*min*) to the steady current widths for some Rossby radius a. Figure 4 compares the numerical steady dispersive solutions for different W, a values for $\Pi = -1$ with the theoretical current widths $Y_\pm$. For small widths the upstream Y_- is close to the theoretical $(Y_-)_{max}$ value. As the outflow width increases from $W = 1$ to $W = 100$ in the $a = 1.3$ case, the current widths converge towards the hydraulic prediction $(Y_-)_{min}$. The full QG solutions for a point source $W = 0$ closely align with the narrow outflow case: in the $W = 1$ dispersive simulations, a shock appears at Y_s where the soliton terminates that matches the current widths for the full problem.

3.3. *The validity of the $W \to 0$ predictions and overturning*

For all width outflows as $t \to \infty$, the time-dependent PV equation chooses Φ (for which all of Y_+, Y_-, $\alpha_\pm$, $E_\pm$ are determined) such that

(i) There is a constant-width current at one of the edges of the source width which stipulates $Y_x(x = -W\Pi) = Y_{xx}(x = -W\Pi) = 0$;

(ii) The flow is critically controlled transitioning from subcritical flow far upstream (Y_-) to supercritical flow far downstream (Y_+), or vice versa depending on the sign of Π. In the hydraulic solution, the current width is critically controlled at the edge of the source width, but this condition is relaxed in the dispersive equation, being true only provided $W \to \infty$. Dispersion means that Φ is a function that is also dependent on the width of the outflow.

Moving from subcritical to supercritical flow in the dispersive equation for $\Pi = +1$ requires $C(Y)|_{Q=0,\ \Pi=+1} \geqslant 0$. This implies $Y \leqslant 0$ upstream for the steady system for all W, and equality is only reached provided $W = \infty$ (i.e., the hydraulic case). The wave always overturns for outflows $W < \infty$ in the full problem seen in §5, but long-wave theory returns single-valued solutions that cannot capture this case. While the hydraulic solution indicates overturning by producing a shock immediately upstream the outflow, the dispersive solution instead allows the coastal front to reach values $Y < 0$. Overturning decreases with increasing outflow width, and this is reflected in the dispersive equation by decreasing how far below the coast the front reaches. Hydraulic solutions are sufficient to determine the current widths of the full problem provided $\Pi = +1$; contrary to dispersive solutions, the full solution indicates that Φ only changes with W when $\Pi = -1$.

In the negative PV case, the $W \to 0$ treatment matches remarkably with the steady dispersive integrations seen in figure 6. As the outflow width decreases, the current widths tend towards the $(Y_\pm)_{W\to 0}$ analytical values seen in the $W = 1$ and $W = 3$ numerical simulations. At $W = 10$ these values align more closely towards the hydraulic widths; and all lie comfortably in the shaded region that represents the range of solutions for any W.

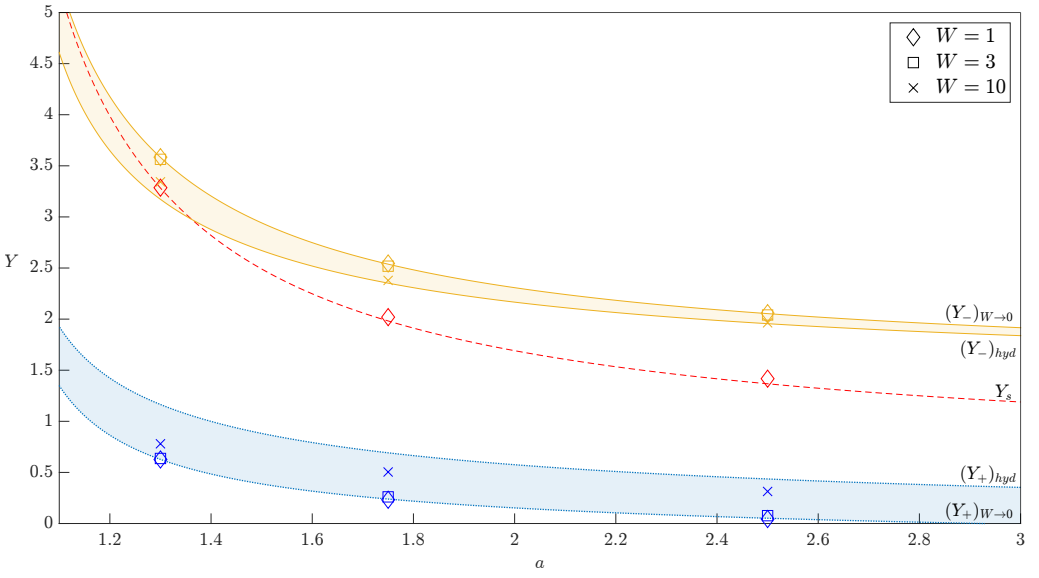

Figure 6: The predicted steady dispersive current widths Y_-, Y_+ at different values of a for $\Pi = -1$. The shaded regions for both Y_+ (lined edge, yellow) and Y_- (dotted edge, blue) show the range of width values based on the outflow width W. The Y_s value (red, dashed) gives the location of the shock for a point source outflow. Also plotted are numerical simulations of the steady dispersive equation at $a = 1.3,\ 1.75,\ 2.5$ at different widths $W = 1,\ 3,\ 10$.

In the $W \to 0$ case, the location of the shock is well predicted by the $W = 1$ numerical steady solution and this is where the $Q = 1$ soliton terminates. The dependence of the outflow width on the range of values $Y_\pm$ is also captured in the full problem provided $\Pi = -1$, detailed in §5.

For sufficiently large Rossby radius a and $\Pi = -1$, the downstream current width Y_+ reaches the coast $Y = 0$. This behaviour is reflected in the full problem that is not found in the hydraulic solution: only as $a \to \infty$ then $Y_+ \to 0$, so the current always reaches the coast via a rarefaction. As it is unphysical for the front to lie underneath the coast, we stipulate that for $a \geqslant a_{turn}$, defining a_{turn} as the point the PV front reaches the coast $Y = 0$, it necessarily follows that

$$Y_+ = 0, \quad Y_- = a \ln\left(\frac{a}{a - \sqrt{2}}\right) \quad \forall\ a\ \geqslant\ a_{turn}. \tag{3.24}$$

Therefore, the current widths for either $\Pi = \pm 1$ from (3.12), (3.24) both tend to $Y_\pm \to \sqrt{2}$ as $a \to \infty$ as in Johnson & McDonald (2006). Following the $W \to 0$ analytical treatment suggests that $a_{turn} \approx 2.96$, which is explicitly compared to the full problem in §5. Thus, the dispersive theory consolidates the hydraulic theory by predicting the steady current widths $Y_\pm$ in all cases of $a,\ W$.

4. The leading frontal regions

4.1. *The time-dependent dispersive long-wave equation*

With the widths Y_+, and Y_- of the currents leaving the source region determined, it remains to consider the propagation of the dispersive fronts leading the currents. Table 1 summarises the notation used below. In order to numerically solve the unsteady dispersive equation (2.12) noting the three spatial derivatives in $Q(x)$, we require that the flux is

Name	Description
Y_+	Constant-width current upstream from source outflow
Y_-	Constant-width current downstream from source outflow
Y_I	Width of intrusion (or half-intrusion) that connects the current width to the coast
s_I	Speed of the intrusion (or half-intrusion)
Y_s	Width of the soliton edge resulting from DSW formation
$\tilde{s}_I$	Speed of the soliton edge
s_r	Speed of the rarefaction at coast $Y = 0$

Table 1: The notation for the different wave structures in the PV front.

sufficiently smooth so that at least the third derivative is bounded. For the integrations below, we use the flux function

$$Q_4(x) := \begin{cases} 0 & x \leqslant -W \\ \frac{8}{9}\sin^4\left(\frac{\pi(x+W)}{3W}\right) & -W < x \leqslant 0 \\ 1 - \frac{8}{9}\sin^4\left(\frac{\pi(x-W)}{3W}\right) & 0 < x < W \\ 1 & x \geqslant W. \end{cases} \tag{4.1}$$

Using $Q(x) := Q_4(x)$ in (4.1) guarantees no discontinuities in the boundary condition (2.4). Simulations were also attempted with simpler functions, but there was very little difference in the results in either the full problem or the dispersive integrations.

A simple fourth-order Runge-Kutta scheme is used to advance the equation in time using a pseudo-spectral method, where the equation is Fourier transformed in x and solved as an ODE in Fourier space, and is then transformed back into real space. The domain we assume is periodic; hence, we require the flux function to also be periodic. In practice, we truncate the domain to $x = L$, $L \gg 1$, and to maintain periodicity, the flux function must also descend to 0 downstream. We make this descent gradual enough as not interfere with the true propagation of the source outflow, in this case, $Q_4(x)$ is stepped down to 0 using a sufficiently wide tanh function. We also apply de-aliasing following Orszag (1971) to remove any exponentially decaying high-wavenumber solutions, eliminating any spurious waves that have a frequency greater than the resolution of the domain.

4.2. *Compound-wave structures and dispersive shock wave fitting*

The structure of the PV front can be seen as a composition of different wave structures discussed in JJ20. Two far-field states can be connected by shock, rarefaction, or compound shock-rarefaction depending on the specific conditions in the hydraulic PV equation (2.9). Compound wave structures occur provided $Q_e(Y)$ is not entirely convex in the region of interest, which means that the interval $[Y_-, Y_+]$ contains a turning point Y_{turn} of $C(Y) := -Q_e'(Y)$ where $C'(Y_{turn}) = 0$; that is, $Y_{turn} \in [Y_-, Y_+]$.

Importantly, the governing dispersive equation also forms compound-wave structures provided $Q_e(Y)$ is not convex. Although rarefactions still occur, far-field states are instead linked by kink-solitons or intrusions analogous to a shock, or by a dispersive shock wave (DSW) provided $Y_+ \neq 0$. Here, a DSW is a wave structure slowly modulated in amplitude and frequency connecting two far-field states with different propagation speeds at each

edge: one being a linear wavepacket and the other a solitary wavepacket. The dispersive shock fitting method (El 2005) that analyses DSW properties is valid if the governing PV equation satisfies a certain set of conditions outlined in the appendix 7.1.

Seeking solutions of the form $Y = Y_\infty + \eta e^{i(kx-\omega t)}$, $\eta \ll \mathcal{O}(1)$ for waves propagating on a background Y_∞, the governing PV equation for constant $Q(x) = Q$ has a linear dispersion relation where $\mathcal{O}(\eta^2)$ terms or higher are ignored given by

$$\omega(k) = C(Y_\infty)k - \frac{a^2\Pi}{4}\mathcal{G}(Y_\infty)k^3, \tag{4.2}$$

where $C(Y) = \left(\frac{Q}{a} + a\Pi\right)e^{-Y/a} - a\Pi e^{-2Y/a}$, $\mathcal{G}(Y) = a - (a+2Y)e^{-2Y/a}$.

We denote the linear-wave-edge wavenumber as k with dispersion relation $\omega(k)$, and the conjugate wavenumber of the solitary-wave edge as $\tilde{k}$, typically defined as the inverse half-width of the solitary wave, with conjugate dispersion relation $\tilde{\omega}(\tilde{\kappa}) = -i\omega(i\tilde{k})$. In this problem the far-field states are given by $Y_I \neq 0$ (the intrusion width) and either Y_-, $Y_+ \neq 0$ according to the sign of the PV Π. We can find the wavenumber or conjugate wavenumber by solving the ODE's derived by El (2005) to obtain JJ20 for general constant $Q(x) = Q$:

$\Pi = -\mathbf{1}$:

$$k_-^2 = \frac{-8}{3a^2\mathcal{G}(Y_-)^{2/3}}\int_{Y_I}^{Y_-}\frac{C'(Y)}{\mathcal{G}(Y)^{1/3}}\,dY, \quad \tilde{k}_I^2 = \frac{8}{3a^2\mathcal{G}(Y_I)^{2/3}}\int_{Y_-}^{Y_I}\frac{C'(Y)}{\mathcal{G}(Y)^{1/3}}\,dY, \tag{4.3}$$

$\Pi = +\mathbf{1}$:

$$k_+^2 = \frac{8}{3a^2\mathcal{G}(Y_+)^{2/3}}\int_{Y_I}^{Y_+}\frac{C'(Y)}{\mathcal{G}(Y)^{1/3}}\,dY, \quad \tilde{k}_I^2 = \frac{-8}{3a^2\mathcal{G}(Y_I)^{2/3}}\int_{Y_+}^{Y_I}\frac{C'(Y)}{\mathcal{G}(Y)^{1/3}}\,dY, \tag{4.4}$$

where k_- is the wavenumber of the linear wave-edge ($\tilde{k}_I = 0$ here), and $\tilde{k}_I$ is the conjugate wavenumber of the solitary wave-edge ($k_- = 0$ here).

Thus, the DSW forms a compound wave structure with the upstream steady current $(Y_-, \Pi = -1)$, where the DSW travels leftward from the linear wave edge at Y_- to the solitary wave edge at Y_I where it connects to an intrusion on the left; or with the downstream steady current $(Y_+, \Pi = +1)$, where the DSW travels rightward from the linear-wave edge at Y_+ to the solitary wave-edge at Y_I where it connects to an intrusion on the right. The propagation speeds of the solitary and linear wave-edges are

$$s_\pm = \frac{\partial\omega}{\partial k}(Y_\pm, k_\pm), \quad \tilde{s}_I = \tilde{\omega}(Y_I, \tilde{k}_I)/\tilde{k}_I, \tag{4.5}$$

computing the speeds and the amplitude of the solitary wave at Y_I, denoted by Y_s, as well as the wavelength of the linear wave at $Y_\pm$. Sections 4.3 and 4.4 give examples of DSWs.

4.3. *The structure of the PV front: the $\Pi = +1$ positive PV case*

4.3.1. *Upstream of the source, $x < -W$: $Q = 0$, $\Pi = +1$*

The upstream flow of $\Pi = +1$ is well captured by the hydraulic theory of JSM17. The flow is led by a shock and terminates at the edge of the source outflow and control point $x = -W$, so $Y_- \equiv 0$, $x \leqslant -W$ for all a. The unsteady dispersive equation is ignored as it gives a poor representation of the upstream flow, predicting negative values to indicate wave overturning as discussed in §3.1.2.

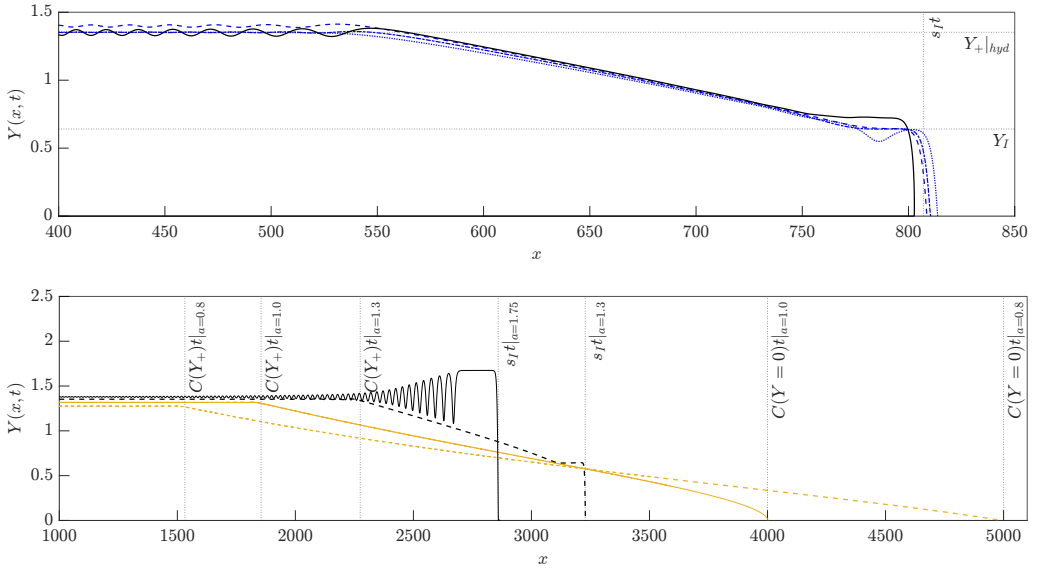

Figure 7: Top: Dispersive solution for $\Pi = +1,\ a = 1.3$ and widths $W = 3,\ 10,\ 20$ (overlaid as blue; dashed, dash-dotted, dotted respectively), compared directly with the point source contour dynamics simulation (black) at time $t = 1000$, focusing on the Y_+ region and upstream. Bottom: Similar to top but for width $W = 10$ and $a = 0.8,\ 1.0,\ 1.3,\ 1.75$ (black, black-dashed, yellow, yellow-dashed respectively) run until $t = 4000$. The dotted lines in both figures correspond to the theoretical predictions of the structure's locations.

4.3.2. *Downstream of the source, $x > W$: $Q = 1$, $\Pi = +1$*

Downstream the source outflow, $x > W$, the flux function $Q_e(Y)$ is always non-convex in the solution if

$$Y_{turn} = a \ln\left(\frac{2a^2}{a^2+1}\right) \geqslant 0. \tag{4.6}$$

For $a < 1$ a rarefaction joins these states and thus we denote $a_{r,\,+1} = 1$ as the value of a when a rarefaction just forms. Equation (4.6) is satisfied provided $a \geqslant 1$, where an intrusion connects the downstream current Y_+ to the coast with a finite slope and current width Y_I determined by (2.16) and (2.18). A rarefaction, if it occurs, propagates according to the equation

$$\frac{x}{t} = C(Y) = \frac{1}{a}\left(1+a^2\right)e^{-Y/a} - ae^{-2Y/a}, \quad C(Y_+) < C(Y) < C(Y = Y_{join}) \equiv \frac{1}{a}, \tag{4.7}$$

where Y_{join} refers to $Y = 0$ if a rarefaction fully joins to the coast, or Y_I if a rarefaction joins to an intrusion instead.

We also require for any soliton or intrusion that the stationary points of Y_ξ in (2.13) must be local minima (representing a stable equilibrium of the far-field states), i.e.

$$\nu''(Y_I) > 0 \implies |s_I| > |C(Y_I)|, \tag{4.8}$$

consequently an intrusion always overtakes a rarefaction and join the far-field state to the coast. This forms a constant-width current region that is referred herein as a "shelf". We can calculate the values for which the shelf is wider or narrower than the immediate downstream current Y_+ by determining when

$$Y_I = (Y_+)_{hyd}. \tag{4.9}$$

List of downstream behaviours according to the value of a ($\Pi = +1$)

Name	Description	Value (2 d.p.)
$a_{r,\,+1}$	Lower limit of a when an intrusion forms	1.00
$a_{I,\,+1}$	Lower limit of a when a DSW forms	1.62
$a_{crit,\,+1}$	Lower limit of a when a constant-width shelf no longer forms	1.99

Table 2: The values of a where different behaviours of the upstream PV front form for $\Pi = +1$.

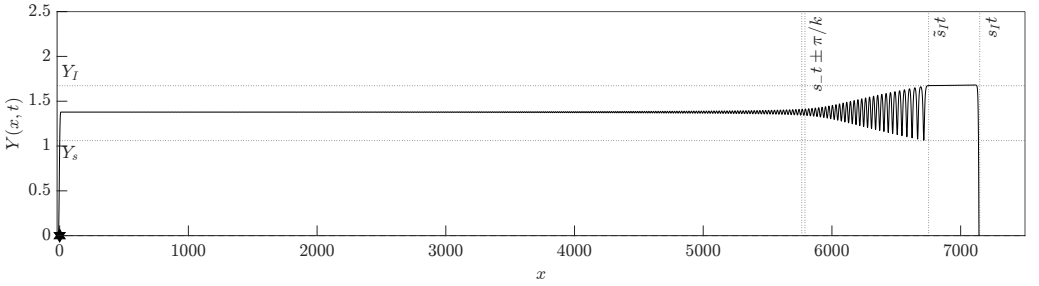

Figure 8: The numerical solution to the governing dispersive equation with $\Pi = +1$ and $a = 1.75$, run until $t = 10000$, showing a DSW propagating upstream. The source outflow centred at $x = 0$ is $Q(x) \equiv Q_4(x)$ with width $W = 10$. The dotted lines represent the predictions of the dispersive analysis using El's technique and travelling-wave solutions.

We denote the value of a for which (4.9) is satisfied by $a_{I,\,+1}$. Then for all $a > a_{I,\,+1}$, the intrusion shelf always remains wider than the constant-width downstream current Y_+, leading to DSW formation. A shelf cannot form if the speed of the leading soliton edge of the DSW $\tilde{s}_I$ matches the speed of the intrusion s_I, which occurs when

$$\tilde{s}_I = s_I. \tag{4.10}$$

We denote the value of a for which (4.10) holds by $a_{crit,\,+1}$. A "half-intrusion" joins the far-field current to the coast for $a > a_{crit,\,+1}$, discussed further in §4.5. The values of $a_{r,\,+1}$, $a_{I,\,+1}$ and $a_{crit,\,+1}$ are given in table 2.

The type of structures that form also vary with the outflow width W in the dispersive equation. However, as noted in §3.3, this is an artefact of the dispersive equation which does not reflect the behaviour of the full problem. Although changing the source width W does not affect Y_+ in the full QG equations, it introduces more waves to the system due to dispersion. Herein, irrespective of W, we only use hydraulic solutions $(Y_+)_{hyd}$ to estimate the actual downstream current width.

Figure 7 (top) shows the numerical differences in the downstream behaviour by comparing the point source $W = 0$ contour dynamics with the dispersive dynamics at widths $W = 3,\ 10,\ 20$ for $a = 1.3$. In the $W = 3$ case, the dispersive dynamics capture the waves propagating upstream the source, but the $W = 10,\ 20$ outflows capture Y_+ better and so the simulations below are restricted, unless noted, to the width $W = 10$ for $\Pi = +1$. This width closely matches to the point source prediction of Y_+, yet is not so large that dispersive waves interfere with the solution (as with $W = 20$). The contour dynamics also matches reasonably well to the predicted intrusion location at $t = 500$ from travelling-wave theory. This is shown further in figure 7 (bottom) where the predicted

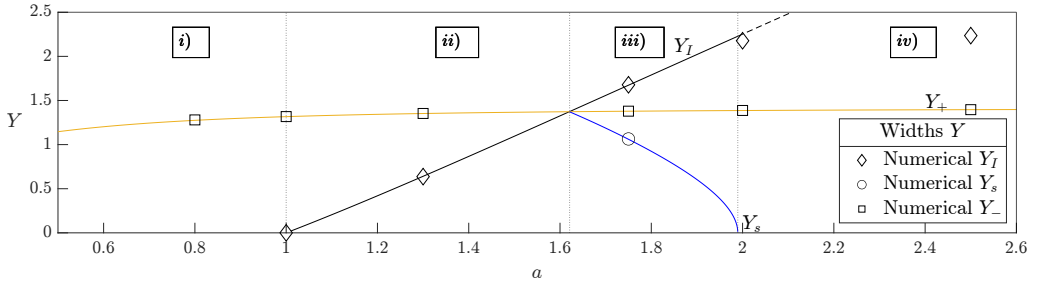

(a)

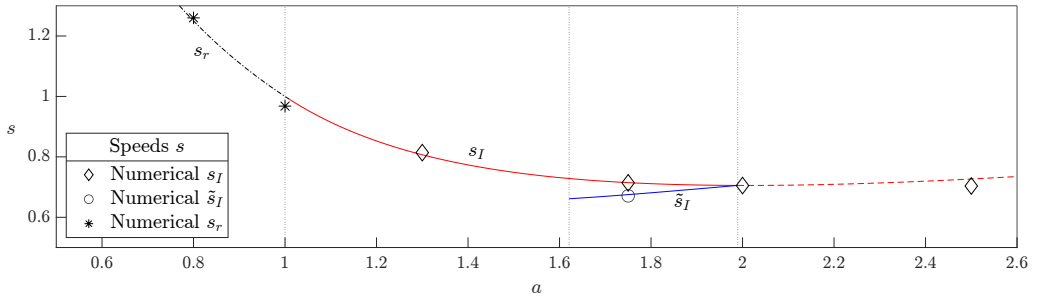

(b)

Figure 9: Downstream behaviour of the dispersive equation for $\Pi = +1$. The numbers i) - iv) describe regions of a where different behaviours of the front occur. (a) The theoretical and numerical ($W = 10$) widths of Y_I (black, plotted diamond), Y_+ (orange, plotted square), and Y_s (blue, plotted circle) if a DSW forms. (b) The respective speeds for s_r (black dash-dotted, plotted stars) s_I (red lined, plotted diamond), $\tilde{s}_I$ (blue, plotted circle). All simulations are run for at least $t \geqslant 1000$ so Y_+ becomes steady.

intrusions, rarefactions $C(Y = 0)$ and long-wave propagation $C(Y = Y_+)$ locations align well at $t = 4000$ for a range of values of a.

We verify El's technique for $a = 1.75 > a_{I,\,+1}$ where DSWs can form. Figure 8 shows a DSW propagating to the right downstream, where there is a rightwards solitary-wave leading edge and a linear-wave trailing edge. A long simulation time ($t = 10000$) is used so that the DSW can be fully developed. The PV front terminates via an intrusion (a kink-DSW structure) with a corresponding width and speed Y_I, s_I that is well matched with the theoretical travelling-wave theory; similarly, the theoretical dispersive shock fitting matches well with the trailing, leading positions and the soliton width at the leading edge $s_- t$, $\tilde{s}_I t$, Y_s. We deduce the linear wave wavelength of the DSW by calculating the distance $2\pi/k_-$, given by the two dotted lines along the trailing edge shown in the figure, again showing good agreement.

In summary,

(i) if $0 \leqslant a \leqslant a_{r,\,+1}$: Y_+ terminates towards the coast by a rarefaction (see figure 7 (bottom), labelled yellow).

(ii) if $a_{r,\,+1} < a \leqslant a_{I,\,+1}$: The PV front from Y_+ terminates towards the coast via an intrusion with current width Y_I, and a compound-wave intrusion-rarefaction joins to the downstream current Y_+. Here $0 < Y_I < Y_+$ (see figure 7 (bottom), labelled black-dashed).

(iii) if $a_{I,\,+1} < a \leqslant a_{crit,\,+1}$: An intrusion terminates towards the coast with current width Y_I, and a compound-wave intrusion-DSW joins to Y_+ for all widths W. Here $0 < Y_+ < Y_I$ (see figure 8).

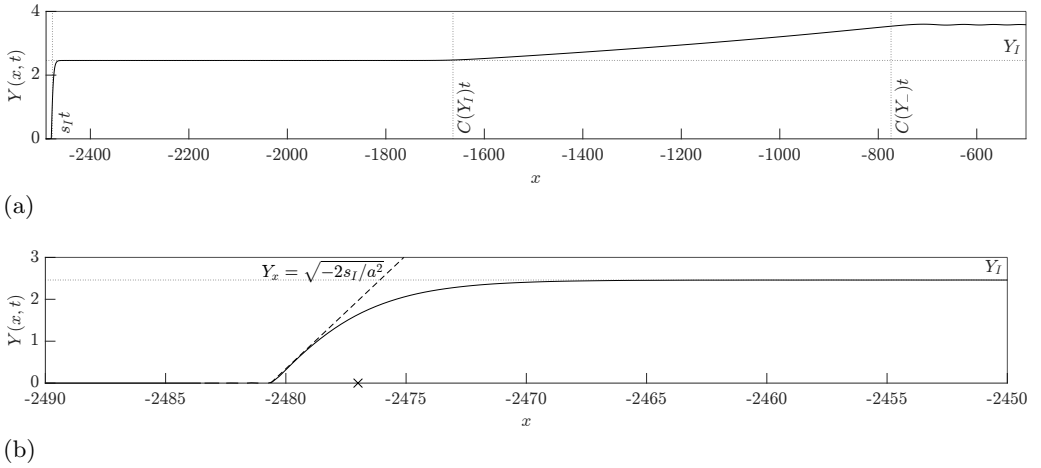

(a)

(b)

Figure 10: (a) The upstream analytical predictions (in dash-dotted) of the rarefaction and intrusion locations and the numerical integrations of the $\Pi = -1$, $a = 1.3$ dispersive equation at $t = 10000$, $W = 3$. (b) The analytical prediction of the gradient of the intrusion, zoomed in from the top figure. Note the gradient line (dashed) is adjusted very slightly from $s_I t$, the predicted intrusion location (marked as a cross $\times$), for clarity of comparison.

(iv) if $a > a_{crit,\ +1}$: a shelf no longer forms, and the upstream current terminates into a "half-intrusion" instead (see figure 14b).

The parameter regimes for these cases are indicated in figure 9 showing the current widths and speeds Y, s of any structures that form according to a in the $W = 10$ dispersive integrations. In all regions $a < a_{crit,\ +1}$ there is good agreement between the theoretical predictions and the numerical simulations for the speeds of the intrusions, solitons and rarefactions (bottom figure). As $a \to 0$ the downstream speed of the rarefaction tends to infinity where simulations become more numerically challenging to run.

If the speed of the intrusion s_I matches with the speed of the soliton edge $\tilde{s}_I$, the soliton edge Y_s reaches the coast and this leads to a change in behaviour. The dispersive equation forms a half-intrusion instead of a standard intrusion that connects the far-field state to the coast provided $a \geqslant a_{crit,\ +1}$. This significantly changes the expected width for the new half-intrusion (shown in dashed lines in figure 9), discussed in §4.5.

4.4. *The structure of the PV front: the $\Pi = -1$ negative PV case*

The structures in the negative PV case are similar to those of the positive PV case but the current widths $Y_\pm$ are also dependent on the source width W and a.

4.4.1. *Upstream of the source, $x < -W$: $Q = 0$, $\Pi = -1$*

Upstream where $Q = 0$, $x < -W$, since $|C(Y = 0)| < |C(Y = Y_-)| \quad \forall\ Y_- > 0$, an intrusion always forms and it is not necessary to satisfy the non-convexity condition for $Q_e(Y)$. This is true even if $a \leqslant 1$ where there are no steady solutions. Unless the intrusion is of the same width as Y_- (analogous to a shock in hydraulic flow), compound-wave structures always appear. Again the intrusion meets the coast with finite slope and current width Y_I predicted using the equations (2.16) and (2.18). Similarly in (4.8) the intrusion satisfies $\nu''(Y_I) > 0$, travelling faster than any rarefaction, so the constant-width shelf formed by the intrusion lengthens over time (in the x-direction) before joining to either a rarefaction or DSW.

List of upstream behaviours according to the value of a ($\Pi = -1$)

Name	Description	Value (2 d.p.)
$a_{lower,\ -1}$	Lower limit of a when a DSW forms ($W \to \infty$)	1.46
$a_{higher,\ -1}$	Lower limit of a when a DSW forms ($W \to 0$)	1.53
$a_{crit,\ -1,\ min}$	Lower limit of a when a constant-width shelf no longer forms ($W \to \infty$)	1.94
$a_{crit,\ -1,\ max}$	Lower limit of a when a constant-width shelf no longer forms ($W \to 0$)	2.02

Table 3: The values of a for the different upstream behaviours of the PV front for $\Pi = -1$.

The equation of a rarefaction provided it forms is given by

$$\frac{x}{t} = C(Y) = ae^{-2Y/a} - ae^{-Y/a}, \quad C(Y_I) < C(Y) < C(Y_-). \tag{4.11}$$

Figure 10 shows a kink-rarefaction structure for $a = 1.3$ and an example of shelf formation in 10(a). The location of the rarefaction is well predicted by long-wave speed calculations $C(Y)$, likewise with the location, width, and instantaneous gradient of the intrusion. Figure 11 gives another example of an (upstream) DSW where its solitary-edge propagates leftward. The discussion of the theoretical predictions (dotted in figure) is identical to the discussion following figure 8 in the positive PV case, with both the predicted locations and widths agreeing well with the dispersive integrations.

Similarly to §4.3.2, we can determine the values of a for which the shelf is as wide as the constant-width current Y_- for long times by determining when

$$Y_I = Y_-, \tag{4.12}$$

and again (4.10) determines when a shelf no longer forms. Since changing the source width leads to two different bounds of Y_-, this also gives two different values of a for when these behaviours occur. These values and their corresponding notation are given in table 3.

In summary,

(i) if $0 \leqslant a \leqslant a_{lower,\ -1}$: The PV front terminates towards the coast via an intrusion with current width Y_I, followed by a rarefaction which joins to the downstream current Y_-. Here $0 < Y_I < Y_-$ (see figure 10 (a)).

(ii) if $a_{lower,\ -1} < a < a_{higher,\ -1}$: Same in (i) for sufficiently large W, otherwise rarefaction-intrusions may also form for sufficiently small width outflows.

(iii) if $a_{higher,\ -1} \leqslant a \leqslant a_{crit,\ -1,\ min}$: An intrusion terminates towards the coast with current width Y_I, followed by a DSW which connects to the downstream current width Y_- for all outflows width W. Here $0 < Y_- < Y_I$ (see figure 11).

(iv) if $a_{crit,\ -1,\ min} < a \leqslant a_{crit,\ -1,\ max}$: This forms the lower (when $W = \infty$) and upper bound (when $W = 0$) of when a shelf can form according to the source width.

(v) if $a > a_{crit,\ -1,\ max}$: a shelf no longer forms for all outflow widths W. Instead, the downstream current terminates towards the coast via a series of modulated, periodic travelling waves, described here as "half-intrusions" (see figure 14b)).

As in the case $\Pi = +1$, changing the width of the outflow produces additional waves forming a range of different phenomena that is not straightforward to quantify. For example, figure 11 (bottom) is identical to the top figure but a large width outflow $W = 100$ is used instead. Using a very large outflow generates waves arising from dispersion that interact with the DSW forming breathers, e.g. Chabchoub *et al.* (2019), which are

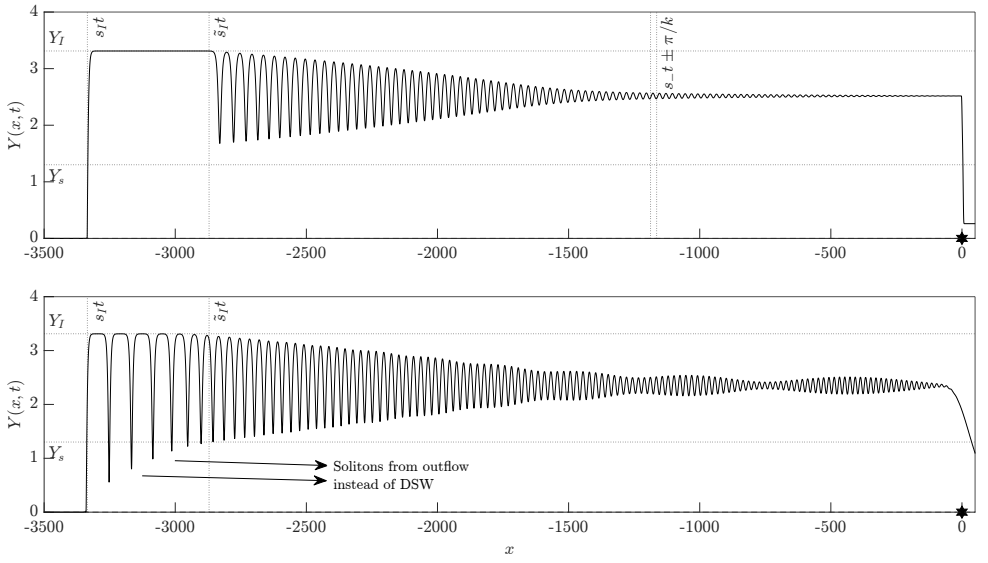

Figure 11: Top: as in figure 8 but with $\Pi = -1$, $a = 1.75$ and $W = 3$, run until $t = 10000$. Bottom: as in top but with a source outflow $W = 100$ run until $t = 10000$. We observe oscillating "breathers" forming upstream inside the DSW.

unsteady nonlinear solutions with internal oscillations. Hoefer *et al.* (2023) analyse an exact solution that generates breathers in the Korteweg-de Vries equation. Further KdV analytical work has determined whether solitons can tunnel through or stay trapped in some form of mean-flow (e.g. a DSW) wave (van der Sande *et al.* 2021). In this example, the waves generated by the outflow interact with the DSW producing breathers where outflow solitons tunnel through the DSW towards the shelf. These become solitons that remain along the shelf, distinct from the solitons formed by the DSW.

Figure 12 shows the corresponding predictions i) - v) describing the structural behaviours as functions of a against the dispersive integrations. The shaded regions give the ranges of Y_s, $Y_-, \tilde{s}_I$ depending on the value of W. There is generally good agreement with the theory for i) to iv) for small and large widths (set to $W = 3$ and $W = 100$) until $a = a_{crit,\,-1,\,min}$ or $a = a_{crit,\,-1,\,max}$ depending on the width of the source. At this point the intrusion appears to reach a maximum width before decreasing again, out of line with the predictions (shown as an increasing dashed line in the top figure). In figure 12(b), this corresponds to the DSW soliton edge speed $\tilde{s}_I$ matching the intrusion speed s_I, forming a a half-intrusion structure described in §4.5.

4.4.2. *Downstream of the source, $x > W$: $Q = 1$, $\Pi = -1$*

From width Y_+, the front always terminates to $Y = 0$ via a rarefaction. The turning point width of $C(Y)$ is always greater than the maximum value of Y_+, given by $(Y_+)_{max}$, or explicitly

$$Y_{turn} = a \ln\left(\frac{2a^2}{a^2-1}\right) > (Y_+)_{max} = a \ln\left(\frac{a^2}{a^2-1}\right). \tag{4.13}$$

This follows that $Y_+ < Y_{turn}$ $\forall$ a and Y_+ can always be joined to the coast by a smooth rarefaction given by

$$\frac{x}{t} = C(Y) = ae^{-2Y/a} + \left(\frac{1}{a} - a\right)e^{-Y/a}, \quad C(Y_+) < C(Y) < C(Y=0) \equiv \frac{1}{a}, \tag{4.14}$$

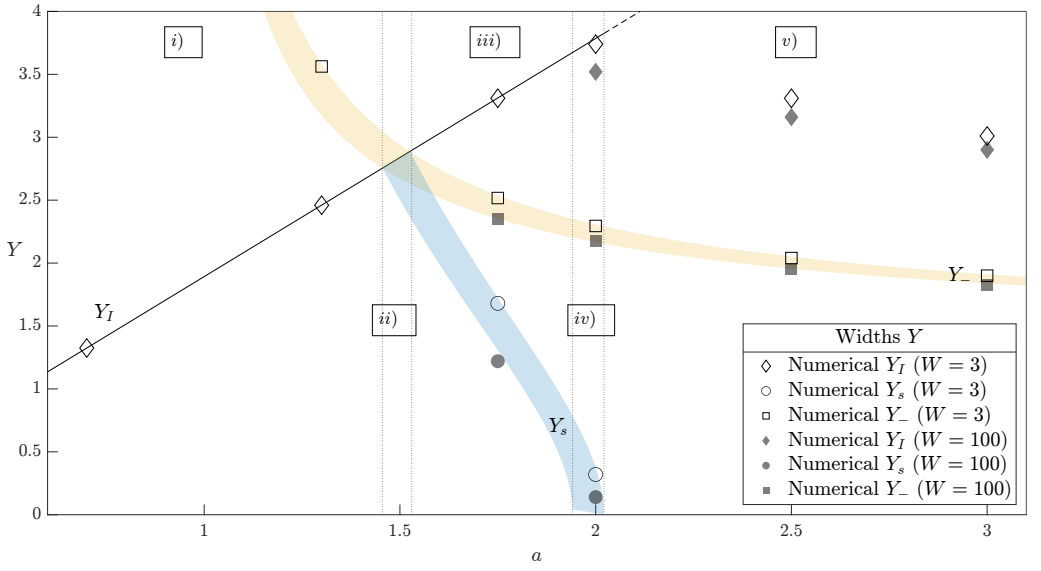

(a)

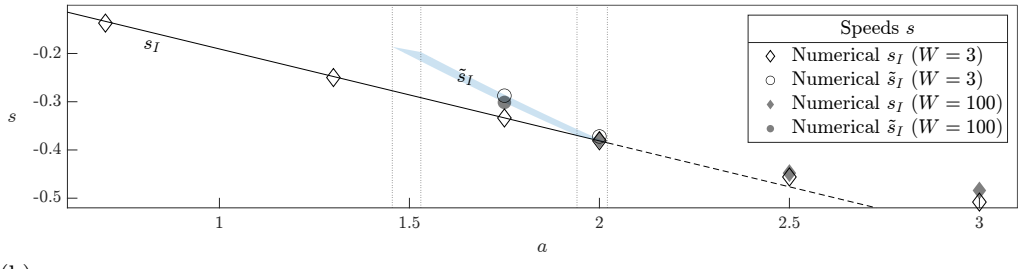

(b)

Figure 12: Upstream behaviour of the dispersive equation for $\Pi = -1$. The numbers i) - v) describe the regions of a where different behaviours of the front occur. (a) The theoretical and numerical widths of Y_I (plotted diamond), Y_- (shaded yellow depending on W), and Y_s if a DSW forms (shaded blue depending on W). (b) The theoretical and numerical speeds of s_I (plotted diamond) and $\tilde{s}_I$ (shaded blue depending on W). All simulations are run for at least $t \geqslant 1000$ so Y_- becomes steady.

provided $Y_+ \neq 0$. Far from the source, the hydraulic terms dominate so any dispersive correction is negligible in determining the rarefaction. In the hydraulic equation $(Y_+)_{hyd}$ is fixed for all widths, and the rarefaction always begins at the control point $x = W$. Figure 13 gives an example of a rarefaction beginning from $x = 0$ given by the blue circle-marked line that corresponds to the fluid being released from the point source $W = 0$. In the dispersive equation, Y_+ is no longer fixed at the control point and is instead a constant-width current propagating at its long-wave hydraulic speed, which then joins to the coast by a rarefaction. This is shown in figure 13 for $a = 1.3$ at $t = 10000$ with the downstream values of Y_+ dependent on the width of the outflow. The locations of the rarefactions, shown by dotted lines in the figure, are well predicted analytically using the predicted steady widths Y_+ ($Y_+|_{hyd}$ is given by (3.11); $Y_+|_{W=0}$ is given by solving (3.19), (3.21), (3.22)). One exception is the $W = 100$ case as the solution has yet to fully settle, and we only begin to see a constant-width current trail emerging. We can

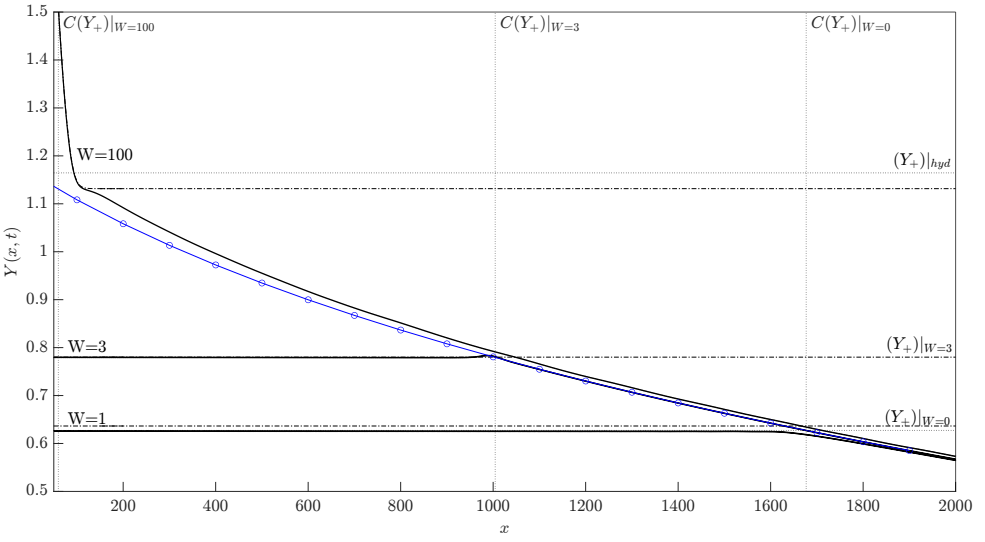

Figure 13: Dispersive integrations of downstream rarefactions for $\Pi = -1,\ a = 1.3$ at $t = 10000$, for widths $W = 1,\ 3,\ 100$ (in black, labelled bottom, middle and top respectively). The blue, circle-marked line gives the $W = 0$ hydraulic rarefaction (4.14). For each W the predicted value of Y_+ is shown dotted and the numerically determined solutions is dot-dashed. The predicted locations (vertical, dotted) on the leading edge of the hydraulic rarefactions are the long-wave speeds for each current width Y_+.

therefore view the dispersive rarefaction as the hydraulic rarefaction truncated at width $Y = Y_+ \leqslant (Y_+)_{hyd}$.

4.5. *Half-intrusion formation and the case $a \gg 1$*

At a critical Rossby radius for $\Pi = \pm 1$ (corresponding to $a = a_{crit,\ +1}$ or certainly after $a = a_{crit,\ -1,\ max}$), the soliton edge reaches the coast $Y = 0$, and the soliton edge matches the speed of the following intrusion. For a coherent structure to persist at larger a, the width of the intrusion and the DSW solitary-edge adjusts itself to join the front at a width where their speeds again match. The structure changes so that the intrusion is replaced by a series of modulated waves meeting the coast, where the last wave is equivalent to a soliton propagating along $Y = 0$ described herein as a "half-intrusion". This modulated travelling wave then joins to the adjusted and truncated DSW, denoted as a partial DSW.

There are studies that analytically determine the widths of the half-intrusions using Riemann invariants in the nonlinear Schrödinger (NLS) piston problem (Hoefer *et al.* 2008). Further observations by Congy *et al.* (2021) categorise these behaviours as part of a "DSW implosion" with multiple regions of behaviour including the formation of a partial DSW in the Benjamin-Bona-Mahony (BBM) equation. They note that a quantitative description of partial DSWs requires significant knowledge of the underlying modulated wave; in the governing PV equation (2.11), it is not straightforward to determine the new adjusted width in this context.

Returning to the potential equation (2.13) and setting

$$\nu(Y = 0) = \nu'(Y = 0) = 0, \quad \nu(Y = Y_I) = 0, \tag{4.15}$$

if the new half-intrusion width Y_I is known, the half-intrusion propagates along the coast with constant speed

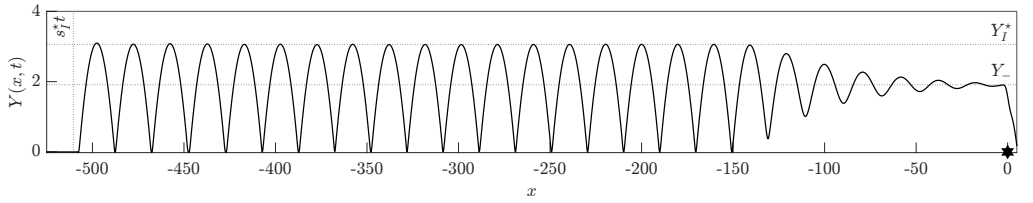

(a)

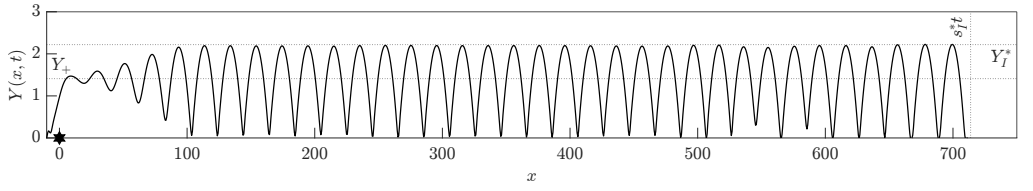

(b)

Figure 14: Upstream DSW behaviour for $W = 3$ source outflows where (a): $a = 3.0$ and $\Pi = -1$ and (b): $a = 6.0$ and $\Pi = +1$ at time $t = 1000$, where a constant-width no longer forms. The predictions for the half-intrusion width and speeds $Y_I^\star,\ s_I^\star$ are detailed in §4.5.

$$s_I^\star = \frac{4a(a^2 + Q\Pi)e^{-Y_I/a} - a^3 e^{-2Y_I/a} + (2a^2 + 4Q\Pi)Y_I - (3a^3 + 4aQ\Pi)}{2\Pi Y_I^2}. \tag{4.16}$$

The travelling wave propagates upstream or downstream with width $Y = Y_I$, and joins to the partial DSW connecting to either Y_-, Y_+. The same is true in reverse where the width $Y_I^\star$ can be obtained given the speed of the wave s_I. Figure 14 shows examples of partial DSWs, where the shelf is replaced by a series of modulated travelling waves reaching the coast. We note that the width of the travelling waves for $a = 3.0$, $\Pi = -1$ is smaller than for instance, $a = 1.75$ in figure 11, departing from when the intrusion width increases if a increases. Equation (4.16) predicts the location of the intrusion well only if the width is known, as seen in the numerical predictions plotted in the figure.

We expect the dynamics of the system for $\Pi = \pm 1$ to be identical except reflected in the y-axis outside of the source width $|x| > W$ by taking

$$x \to -x, \quad \Pi \to -\Pi, \quad a \to \infty.$$

One problem in testing this regime as $a \to \infty$ is that the asymptotic validity of the governing PV equation also begins to break down as $a \gg 1/\varepsilon$, or when a becomes (infinitely) larger than the width of the outflow. After $a = a_{crit,\ +1}$, numerical simulations tested up to $a = 6.0$ in figure 9 (bottom figure) show that the width of the half-intrusion is relatively constant, although it is unclear whether this holds for larger a. If true, we also expect the half-intrusion to have same constant width for $\Pi = -1$.

As we expect $C(Y_\pm) \to \sqrt{2}$ as $a \to \infty$ this stipulates that the half-intrusion width $Y_I > 3\sqrt{2}$, but this does not hold. Indeed, a steady solution may no longer exist in the dispersive long-wave regime $a \to \infty$. As a becomes large the deformation term $-\frac{1}{a^2}\psi$ becomes negligible and the governing equation reduces to Laplace's equation. The PV equation governing the coastal front would include a non-local Hilbert operator instead, significantly altering the flow dynamics (Clarke & Johnson 1997). In fact, Johnson & McDonald (2006) find exact steady solutions to this problem that align with the full QG solutions, suggesting that the asymptotic expansion falters in the limit when a becomes too large.

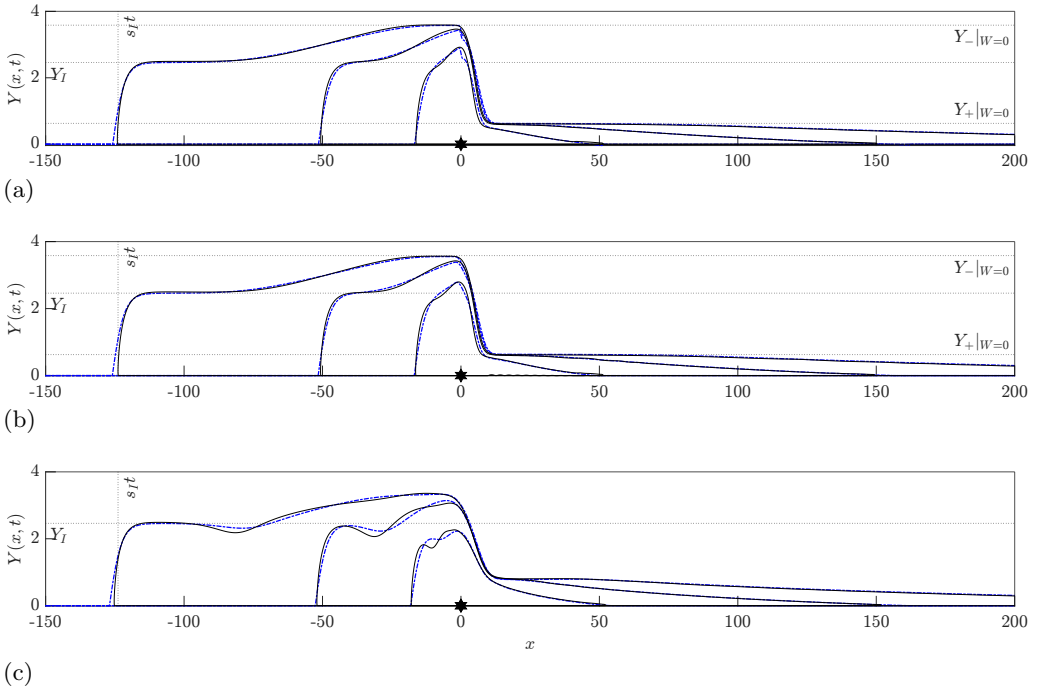

Figure 15: Numerical simulations of the contour dynamics (black) and the dispersive long-wave integrations (blue, dash-dotted) for negative PV outflows $\Pi = -1$, Rossby radius $a = 1.3$ at $t = 60,\ 200,\ 500$, with the flux function $Q(x) := Q_4(x)$ for different widths: (a) $W = 1$, (b) $W = 3$, and (c) $W = 10$. In (a), (b) the theoretical dispersive long-wave $W = 0$ values of the current widths $Y_-|_{W=0},\ Y_+|_{W=0}$ (dotted) are overlaid for comparison, along with the theoretical intrusion widths and locations for all figures.

5. The full problem

With the structure of solutions to the dispersive equation considered we can now compare the long-wave evolution solutions with contour-dynamical evolutions. The full QG solution (2.3), (2.4), (2.5), (2.6) is numerically solved to a high level of accuracy using the contour dynamics method (CD) with surgery following Dritschel (1988). Solving (2.3) involves the Green's function using the modified Bessel function $K_0(r/a),\ r = \sqrt{x^2 + y^2}$ following JJ20, which is further modified by introducing a source outflow along the wall. The velocity profiles associated with the $Q(x) = Q_4(x)$ source outflow are computed in appendix §7.2 while the velocity profile of the point source is given in Southwick *et al.* (2017).

Figure 15 shows for $a = 1.3,\ \Pi = -1$ the improvement of the present dispersive solution over the hydraulic solution in JSM17. In JSM17, hydraulic rarefactions downstream the outflow matched closely with the contour dynamics, and this is also captured by the dispersive integrations. Moreover, there is significantly greater agreement with the current widths adjacent to the outflow $Y_\pm$ than with the hydraulic solutions $(Y_\pm)_{hyd}$. Over long times $t = 500$, the solution converges to the steady solution where a constant-width current Y_- forms just outside the source outflow upstream $x = -W$, followed by a narrower constant-width current downstream Y_+ that meets the coast via a rarefaction. This is consistent with the contour dynamics. When $W = 1$ (figure 15, top) the long-wave asymptotics produces a steep shock-like structure in the source outflow region as predicted by §3.2. The smaller-width sources $W = 1,\ 3$ agree remarkably with the

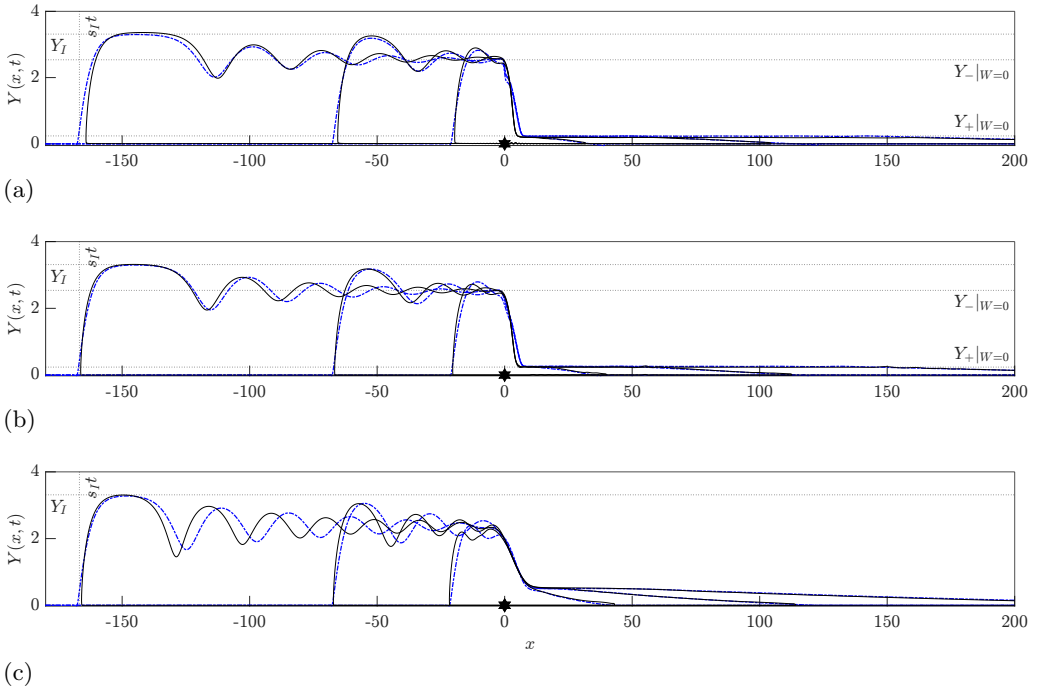

Figure 16: As in figure 15 but with Rossby radius $a = 1.75$ at $t = 60,\ 200,\ 500$ for: (a) $W = 1$, (b) $W = 3$, and (c) $W = 10$. Here, the width Y_I of the intrusion is wider than the width Y_- of the flow immediately upstream outside the outflow.

predicted currents Y_-, Y_+ of the point source contour dynamics $W = 0$ (omitted from the figure because it is graphically indistinguishable from the $W = 1,\ 3$ simulations), agreeing with the $W = 1$ integrations to two decimal places. Only when the width is larger ($W = 10$) do the theoretical hydraulic predictions match more closely with the contour dynamics as in the steady solutions of §3.1. The dispersive equation also accurately predicts the formation of the shelf and the location of the intrusion.

Figure 16 shows an example where the shelf is wider than Y_-, with reasonable agreement with the full problem. For larger widths ($W = 10$), DSWs increasingly become out of phase with the full QG solutions, although the locations of their intrusions remain largely unchanged. This is because the initial contour that forms the front is set up with an initial outflow width equal (or slightly larger) to W, improving the numerical stability, but the dispersive solutions always propagate from $x = 0$. Again, the $W = 0$ point source solutions are graphically indistinguishable from the $W = 1,\ 3$ solutions.

There is also good agreement with the full problem in the $\Pi = +1$ case although less strongly than for the negative PV case. The full solutions always overturn from the outflow, causing the dispersive PV front to lie below the coast to negative Y values. This effect is most prominently seen for smaller widths in figure 17(a). The initial width of the contour is set larger than the actual source width W to prevent the overturning from breaking the contour segments in the contour dynamics, but this (initially) widens the width of the upstream current before it can settle to its true value. Simulations still generally give good quantitative downstream behaviour, especially at longer times $t = 500$. For all widths W, the contour dynamics chooses the current width as $Y_+ \equiv (Y_+)_{hyd}$.

The locations of the intrusions are better predicted for the smaller width outflows. While the intrusion speeds remain identical for all outflow widths, increasing W alters

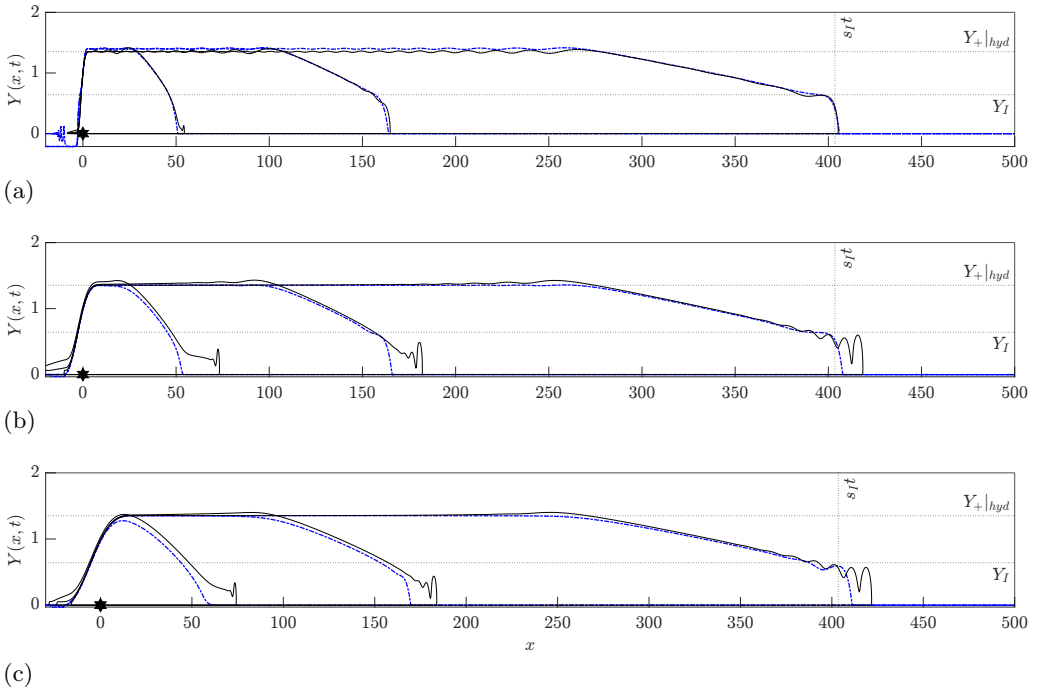

Figure 17: As in figure 15 but with $\Pi = +1,\ a = 1.3$ dispersive solutions (blue, dash-dotted) overlaid with contour dynamics (black, lined) at $t = 60,\ 200,\ 500$ for: (a) $W = 3$, (b) $W = 10$, and (c) $W = 20$.

the magnitude of overturning and increases how far the impulsively started outflow can initially propagate. The appearance of dispersive waves toward the coast becomes more pronounced in the wider outflows, although there is very little dispersion (where waves are virtually constant width) immediately upstream the source. Figure 18 compares the contour dynamics for the $W = 10$ outflows to the dispersive integrations with almost no difference in the case $a = 1.0$. In all cases, the full solution terminates via a rarefaction or intrusion corresponding to the predictions of the dispersive equation.

Beyond $a = a_{crit,\ +1} \approx 1.99$, a shelf no longer appears in the full solution; instead, a series of travelling waves that reach the coast begin to emerge. Again for larger a values the DSW's become out of phase, but the final positions of the intrusions for both $a = 1.75,\ 2.0$ match well with the predicted dispersive locations $s_I t$, $t = 500$; true even at shorter times $t = 200$. The point source $W = 0$ contour dynamics simulations also agree with the final coastal positions and Y_+ with the $W = 10$ dispersive integrations. The only difference is that the wave immediately overturns from the source $x = 0$.

Finally, the regime is numerically tested at $a = 2.5$, where half-intrusions begin to form for $\Pi = \pm 1$ in both the point source and finite-width source regimes. Simulations are run for shorter times $t = 250$ to mitigate eddy formation in the contour dynamics present in figure 19. For larger a values, the solutions align more closely to Johnson & McDonald (2006), where the positive and negative PV solutions are identical but reversed along the x axis. The top figure is simulated using a lower resolution leading to a partial separation of the contours, but using a higher resolution would introduce more eddies to the PV front.

Although the predicted dispersive current widths $Y_+,\ Y_-$ are still captured in the full problem, the widths of the intrusion from the dispersive integrations are underestimated

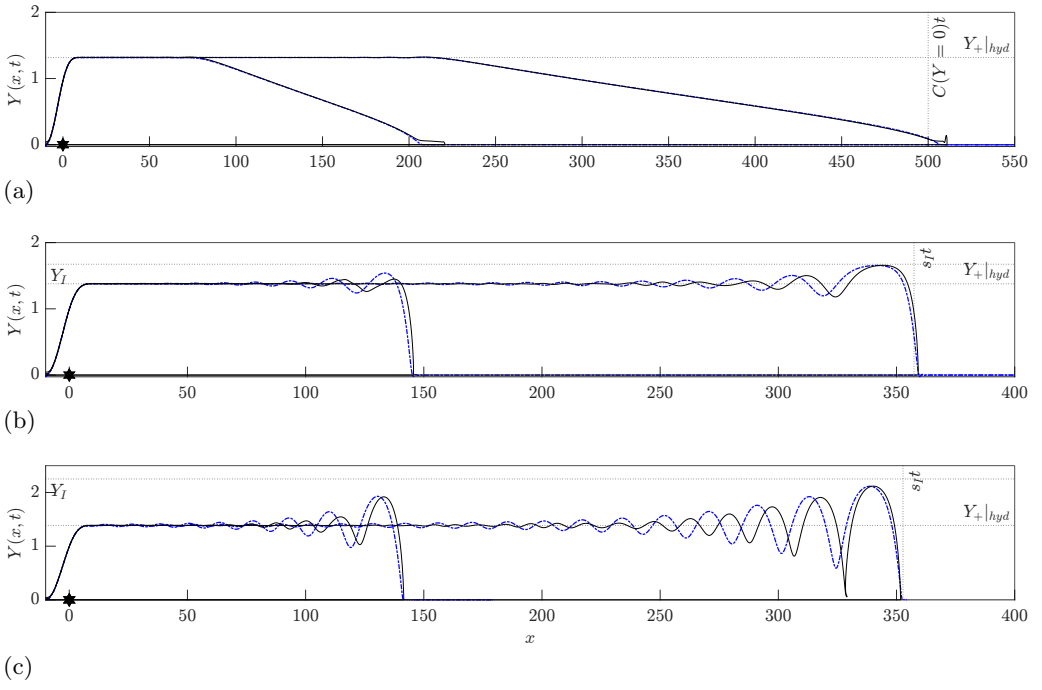

Figure 18: Dispersive integrations of the $\Pi = +1$ regime (blue, dash-dotted) at different Rossby radii $a = 1.0,\ 1.75,\ 2.0$ corresponding to (a), (b), (c) respectively at $t = 200,\ 500$, with source outflow width $W = 10$ are compared with the corresponding contour-dynamics (black, lined). Any theoretical predictions are given as dotted lines. The point source contour dynamics is also given as a comparison with the other solutions (black, dashed).

in both PV regimes. The full QG solutions also form half-intrusions but the last structure is significantly larger than the previous waves. This is due to eddy formation caused by the competition of the velocities between the impulsively started outflow and its subsequent propagation. We also see wave overturning in the negative PV case predicted in §3.3 provided $a_{turn} \approx 2.96$, whereas the full QG solution predicts $a_{turn} \approx 2.5$, a satisfactory estimate. The difference in the overturning predictions explains why the dispersive integrations and contour dynamics end downstream at different points in the $a = 2.5,\ W = 3$ simulations. The full problem likely overturns where the current Y_+ would join to a rarefaction. However, figure 19 (bottom) shows that $C(Y_+)t$ is still far away from where the $W = 3$ contour dynamics terminates downstream. Longer times are required for the solution to adjust to its steady state and achieve better agreement.

6. Discussion

JSM17 discussed the leading-order hydraulic behaviour (in the limit of large outflow width compared to current width) of coastal outflows and compared hydraulic solutions with accurate contour dynamics simulations of the governing QG equation. Although hydraulic solutions captured much of the flow behaviour, there were significant differences in some parameter regimes.

Here, we have continued the expansion to higher order, obtaining a nonlinear, dispersive, long-wave equation for the evolution of the front. At large times, the flow behaviour divides naturally into three regimes: a steady outflow region (§3), steady constant width

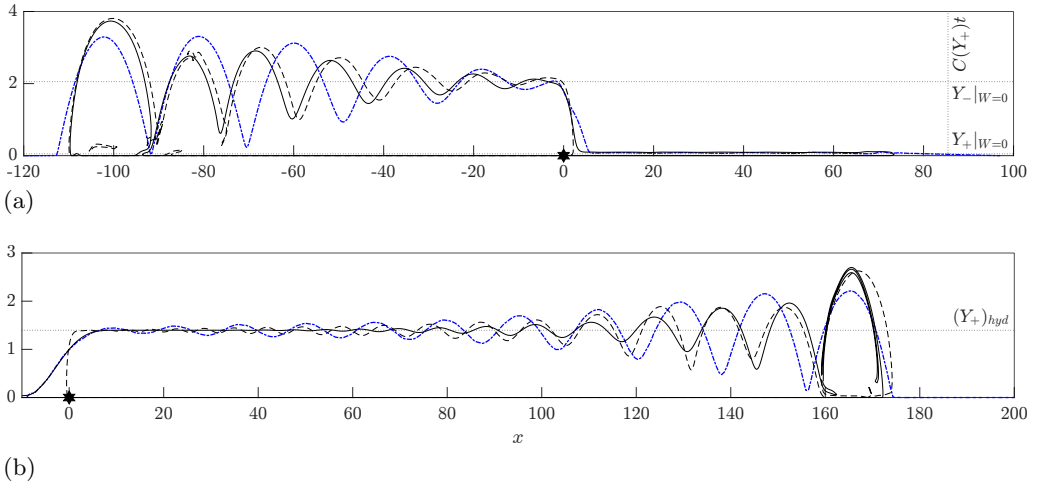

Figure 19: Dispersive integrations for the $a = 2.5$ regime (blue, dash-dotted) with source outflow (a): $W = 3$, $\Pi = -1$; and (b): $W = 10$, $\Pi = +1$ compared to the corresponding contour-dynamics (black, lined) at $t = 250$. Any theoretical predictions are given as dotted lines. The point source contour dynamics at $a = 2.5$ corresponding to the PV is also given as a comparison with the other solutions (black, dashed).

currents joined to the outflow region directly or through a truncated soliton (§3.1, §3.2), and terminating unsteady propagating fronts, influenced strongly by dispersive effects (§4).

The widths of the steady currents are a strong function of the dispersion when the outflow PV anomaly is negative. Here, the upstream steady current width, Y_-, is widest and the downstream steady current width, Y_+, is narrowest for a point source outflow. By adding dispersive terms, we identify wave overturning in the negative PV case (§3.3) that is absent in the hydraulic solutions. This overturning is characterised by regions of negative Y values in the frontal width.

The numerical integrations of the dispersive equation capture the full QG dynamics more accurately than the hydraulic equation, obtaining new behaviour for positive PV (§4.3) and accurate predictions for the downstream current widths in the case of negative PV flows (§3.2). A rich set of behaviours, including dispersive shock wave (DSW) formation and compound-wave structures (rarefaction-intrusions, DSW-intrusions) observed in the QG simulations, are discussed and quantified using standard analysis techniques for nonlinear equations (§4.2, El (2005), JJ20) along with a novel shock-soliton solution (§3.2). For sufficiently large a the dispersive equation admits travelling waves terminating in a half-intrusion (§4.5).

For large internal Rossby radius a, the deformation term in (2.3) becomes negligigble and the governing equation derived here no longer applies. Johnson & McDonald (2006) discuss this limit but present no analytical evolution theory and so consideration of hydraulic and dispersive effects in near-rigid-interface flows remains an area for further exploration.

Decleration of interests

The authors report no conflict of interest.

7. Appendix

7.1. *Conditions for dispersive shock fitting*

In §4.2 we describe the method to ascertain the properties of a DSW that connects two current widths in the regions of constant flux $Q(x) = Q$. Here we briefly describe, adapted from JJ20, the conditions that the governing PV equation must satisfy for this method to successfully apply:

(i) The equation has a hydraulic (zeroth order) limit when we introduce $X = \varepsilon x$ and $T = \varepsilon t$ (this is done in equation (2.9)).

(ii) The linear dispersion relation is real valued, given by (4.2).

(iii) The system possesses at least two conservation laws. The first is equation (2.12) for $Q(x) = Q$ constant Q. The second conservation law for constant $Q(x) \equiv Q$, is from JJ20 (for $Q = 1$). Multiplying (2.12) by Y and simplifying gives

$$0 = \left(\frac{Y^2}{2}\right)_t + \left[\frac{a^2\Pi}{4}(2Y + a)e^{-2Y/a} - (Y + a)(Q + a^2\Pi)e^{-Y/a}\right]_x + \left[\frac{-a^3\Pi}{8}(Y_x^2 - 2YY_x) + \frac{a\Pi}{8}\left[4(Y^2Y_x^2 + \frac{a}{2}YY_x^2) + a^2(Y_x^2 - 2YY_{xx}) - 4aY^2Y_{xx}\right]e^{-2Y/a}\right]_x. \tag{7.1}$$

(iv) The equation supports periodic travelling-wave solutions parameterised by three independent variables. This is shown when writing the PV equation in potential form (2.13).

(v) Considering slowly modulating (changing) waves means that we are able to obtain the Whitham system, which is a set of equations involving our two conservation laws (averaged over the period of a typical travelling wave) plus the wavenumber conservation equation $\omega_x + k_t = 0$. This system must be hyperbolic. Since the flux function $Q_e(x, t)$ is non-convex, for certain intervals of Y the system may not be strictly hyperbolic and compound-wave structures form instead.

7.2. *The outflow velocities of the full QG equations*

The streamfunction involved in the zero PV part of (2.3), i.e. $\nabla^2\psi - 1/a^2\psi = 0$, is found by considering the velocity of the source outflow only. Southwick *et al.* (2017) represent the associated horizontal velocity profiles (u, v) by solving the full solution in appendix B for a general source profile as

$$\begin{pmatrix} u \\ v \end{pmatrix} = \begin{pmatrix} -\partial\psi/\partial y \\ \partial\psi/\partial x \end{pmatrix} = \frac{1}{\sqrt{2\pi}} \int_{-\infty}^{\infty} \begin{pmatrix} \kappa \\ ik \end{pmatrix} \hat{Q}(k) e^{-\kappa y} e^{ikx}\, dk, \tag{7.2}$$

where $\hat{Q}(k)$ is the Fourier-transform of the source $Q(x)$. We construct the outflow $Q_4(x)$ to be symmetric in x, so that the following horizontal velocities are odd:

$$u = \frac{1}{2a}e^{-y/a} + \frac{1}{\pi}\int_0^\infty \frac{\kappa e^{-\kappa y}\sin(kx)}{k}\,dk$$
$$-\frac{1}{\pi}\int_0^\infty \kappa e^{-\kappa y}\left(\frac{\sin(kx)\left(1458k^4W^4 - 3240\pi^2k^2W^2 - 768\pi^4\left(\cos(kW)-1\right)\right)}{18(81k^5W^4 - 180\pi^2k^3W^2 + 64\pi^4k)}\right)\,dk, \tag{7.3}$$

$$v = \frac{1}{\pi}\int_0^\infty e^{-\kappa y}\cos(kx)\,dk$$
$$-\frac{1}{\pi}\int_0^\infty \frac{k\cos(kx)\left(1458k^4W^4 - 3240\pi^2k^2W^2 - 768\pi^4\left(\cos(kW)-1\right)\right)}{18(81k^5W^4 - 180\pi^2k^3W^2 + 64\pi^4k)}\,dk. \tag{7.4}$$

This gives the velocity profiles of an outflow source of width W used in the contour dynamics to solve the full QG equation in §5.

REFERENCES

Ajani, P., Davies, C., Eriksen, R. & Richardson, A. 2020 Global warming impacts Micro-Phytoplankton at a long-term Pacific Ocean coastal station. *Frontiers in Marine Science* **7**.

Chabchoub, A., Mozumi, K., Hoffmann, N., Babanin, A. V., Toffoli, A., Steer, J. N., van den Bremer, T. S., Akhmediev, N., Onorato, M. & Waseda, T. 2019 Directional soliton and breather beams. *Proceedings of the National Academy of Sciences* **116** (20), 9759–9763.

Clarke, S. R. & Johnson, E. R. 1997 Topographically forced long waves on a sheared coastal current. part 2. finite amplitude waves. *Journal of Fluid Mechanics* **343**, 153–168.

Congy, T., El, G. A., Hoefer, M. A. & Shearer, M. 2021 Dispersive Riemann problems for the Benjamin–Bona–Mahony equation. *Studies in Applied Mathematics* **147** (3), 1089–1145, arXiv: https://onlinelibrary.wiley.com/doi/pdf/10.1111/sapm.12426.

Dritschel, D.G. 1988 Contour surgery: A topological reconnection scheme for extended integrations using contour dynamics. *Journal of Computational Physics* **77** (1), 240–266.

El, G. A. 2005 Resolution of a shock in hyperbolic systems modified by weak dispersion. *Chaos: An Interdisciplinary Journal of Nonlinear Science* **15** (3).

Hoefer, M. A., Ablowitz, M. J. & Engels, P. 2008 Piston dispersive shock wave problem. *Phys. Rev. Lett.* **100**, 084504.

Hoefer, M. A., Mucalica, A. & Pelinovsky, D. E. 2023 KdV breathers on a cnoidal wave background. *Journal of Physics A: Mathematical and Theoretical* **56** (18), 185701.

Holliday, N., Bersch, M., Berx, B., Chafik, L., Cunningham, S., Florindo-López, C., Hátún, H., Johns, W., Josey, S., Larsen, K., Mulet, S., Oltmanns, M., Reverdin, G., Rossby, T., Thierry, V., Valdimarsson, H. & Yashayaev, I. 2020 Ocean circulation causes the largest freshening event for 120 years in Eastern Subpolar North Atlantic. *Nature Communications* **11**.

Jamshidi, S. & Johnson, E.R. 2021 Hydraulic control of continental shelf waves. *Journal of Fluid Mechanics* **917**, A4.

Jamshidi, S. & Johnson, E. R. 2019 Coastal outflow currents into a buoyant layer of arbitrary depth. *Journal of Fluid Mechanics* **858**, 656–688.

Jamshidi, S. & Johnson, E. R. 2020 The long-wave potential-vorticity dynamics of coastal fronts. *Journal of Fluid Mechanics* **888**, A19.

Johnson, E. R. & McDonald, N. R. 2006 Vortical source-sink flow against a wall: The initial value problem and exact steady states. *Physics of Fluids* **18** (7), 076601.

Johnson, E. R., Southwick, O. R. & McDonald, N. R. 2017 The long-wave vorticity dynamics of rotating buoyant outflows. *Journal of Fluid Mechanics* **822**, 418–443.

Kida, S. & Yamazaki, D. 2020 The mechanism of the freshwater outflow through the Ganges-Brahmaputra-Meghna delta. *Water Resources Research* **56** (6), e2019WR026412.

Li, J., Roughan, M., Kerry, C. & Rao, S. 2022 Impact of mesoscale circulation on the structure of river plumes during large rainfall events inshore of the East Australian current. *Frontiers in Marine Science* **9**.

Luo, Z., Zhu, J., Wu, H. & Li, X. 2017 Dynamics of the sediment plume over the Yangtze bank in the Yellow and East China seas. *Journal of Geophysical Research: Oceans* **122** (12), 10073–10090.

Mestres, M., Sánchez-Arcilla, A. & Sierra, J. P. 2007 Modeled Dynamics of a Small-scale River Plume under Different Forcing Conditions. *Journal of Coastal Research* **2010** (10047), 84–96.

Orszag, SA 1971 Elimination of aliasing in finite-difference schemes by filtering high-wavenumber components. *Jopurnal of the Atmospheric Sciences* **28** (6), 1074–&.

Piecuch, G. C., Bittermann, K., Kemp, Andrew C., Ponte, Rui M., Little, Christopher M., Engelhart, Simon E. & Lentz, Steven J. 2018 River-discharge effects on United States Atlantic and Gulf coast sea-level changes. *Proceedings of the National Academy of Sciences* **115** (30), 7729–7734.

Pratap, S. & Markonis, Y. 2022 The response of the hydrological cycle to temperature changes in recent and distant climatic history. *Progress in Earth and Planetary Science* **9** (1), 30.

Rahmstorf, S. 2003 Thermohaline circulation: The current climate. *Nature* **421**, 699.

van der Sande, K., El, G. A. & Hoefer, M. A. 2021 Dynamic soliton–mean flow interaction with non-convex flux. *Journal of Fluid Mechanics* **928**, A21.

Southwick, O. R., Johnson, E.R & McDonald, N. R. 2017 Potential vorticity dynamics of coastal outflows. *Journal of Physical Oceanography* **47** (5), 1021 – 1041.

Sun, Y., Youn, S-H., Oh, H., Joo, H-T, Yejin, K., Kang, J., Dabin, L., Kim, K., Jang, H. K., Jo, N., Yun, M., Sun, L. & Lee, S. 2022 Spatial and temporal distribution of phytoplankton community in relation to environmental factors in the southern coastal waters of Korea. *Frontiers in Marine Science* **9**, 950234.

Tao, B., Tian, H., Ren, W., Yang, J., Yang, Q., He, R., Cai, W. & Lohrenz, S. 2014 Increasing Mississippi river discharge throughout the 21st century influenced by changes in climate, land use, and atmospheric CO_2. *Geophysical Research Letters* **41** (14), 4978–4986.

Wang, T., Zhao, S., Zhu, L., McWilliams, J., Galgani, L., Md Amin, R., Nakajima, R., Jiang, W. & Chen, M. 2022 Accumulation, transformation and transport of microplastics in estuarine fronts. *Nature Reviews Earth and Environment* **3**, 795–805.